Bohnsack *et al. Geotherm Energy* (2020) 8:12
https://doi.org/10.1186/s40517-020-00166-9

Geothermal Energy

RESEARCH Open Access

Porosity–permeability relationship derived from Upper Jurassic carbonate rock cores to assess the regional hydraulic matrix properties of the Malm reservoir in the South German Molasse Basin

D. Bohnsack[1], M. Potten[1], D. Pfrang[1], P. Wolpert[1,2] and K. Zosseder[1*]

*Correspondence: kai.zosseder@tum.de
[1] Techincal University Munich, Arcisstr. 21, 80333 Munich, Germany
Full list of author information is available at the end of the article

Abstract

For the successful realization and productivity prediction of new hydrothermal projects in the South German Molasse Basin, the hydraulic matrix properties of the Upper Jurassic Malm reservoir have to be determined as accurately as possible. To obtain specific information on the distribution of the petrophysical parameters (e.g., rock density, porosity, and permeability) 363 samples of rare drilling cores from the reservoir northeast of Munich (wells Moosburg SC4 and Dingolfing FB) were investigated using different experimental methods. Additionally, porosity was calculated by a downhole resistivity log of a nearby borehole close to Munich for comparison and the attempt of transferability of the data set to other locations within the Central Molasse Basin. Core data were divided into groups of different stratigraphic and petrographic units to cover the heterogeneity of the carbonate aquifer and provide data ranges to improve reservoir and prediction models. Data for effective porosity show a high variance from 0.3 to 19.2% throughout this heterogeneous aquifer. Permeability measured on core samples is scattered over several orders of magnitude (10^{-4}–10^{2} mD). Permeability models based on the porosity–permeability relationship were used to estimate permeability for the whole aquifer section and identify possible flow zones. A newly developed empirical model based on distinct lithofacies types allows a permeability estimation with a deviation < 10 mD. However, fractured, karstified, and vuggy zones occurring in this typically karstified, fractured, and porous reservoir cannot yet be taken into account by the model and result in an underestimation of permeability on reservoir scale. Overall, the dominant permeability trends can be mapped well using this model. For the regional transfer and the correlation of the results, a core-related porosity/permeability log for the reservoir was compiled for a well close to Munich showing similarities to the core investigations. The validation of the regional transferability of the parameter set to other locations in the Molasse Basin was carried out by correlation with the interpreted log data of a well near Munich.

Keywords: Porosity, Permeability, Malm, Geothermal energy, Hydraulic properties, Molasse Basin, Carbonate

Springer Open

© The Author(s) 2020. This article is licensed under a Creative Commons Attribution 4.0 International License, which permits use, sharing, adaptation, distribution and reproduction in any medium or format, as long as you give appropriate credit to the original author(s) and the source, provide a link to the Creative Commons licence, and indicate if changes were made. The images or other third party material in this article are included in the article's Creative Commons licence, unless indicated otherwise in a credit line to the material. If material is not included in the article's Creative Commons licence and your intended use is not permitted by statutory regulation or exceeds the permitted use, you will need to obtain permission directly from the copyright holder. To view a copy of this licence, visit http://creativecommons.org/licenses/by/4.0/.

Introduction

Due to its relatively high temperature and promising hydraulic conditions, the Upper Jurassic Malm aquifer buried within the Molasse Basin is the main target formation for geothermal (hydrothermal) exploration in South Germany (Steiner et al. 2014). The Molasse Basin, extending along the northern flank of the Alps as far north as the Franconian Alb, represents an alpine foreland basin (Fig. 1a). In the proximity of Munich, the basin offers ideal conditions for the use of geothermal (hydrothermal) energy to cover the increasing demand for renewable heat sources in Germany. Hence, the Energy Supplier SWM Services GmbH of Munich announced the ambitious goal to cover the heat demand of the city CO_2-emission free until 2040 based on geothermal use (Dufter et al. 2018).

The Molasse Basin itself is filled with Cenozoic sedimentary rocks, which are mostly alternating sequences of sandstone with claystone that overlie and locally cut down into

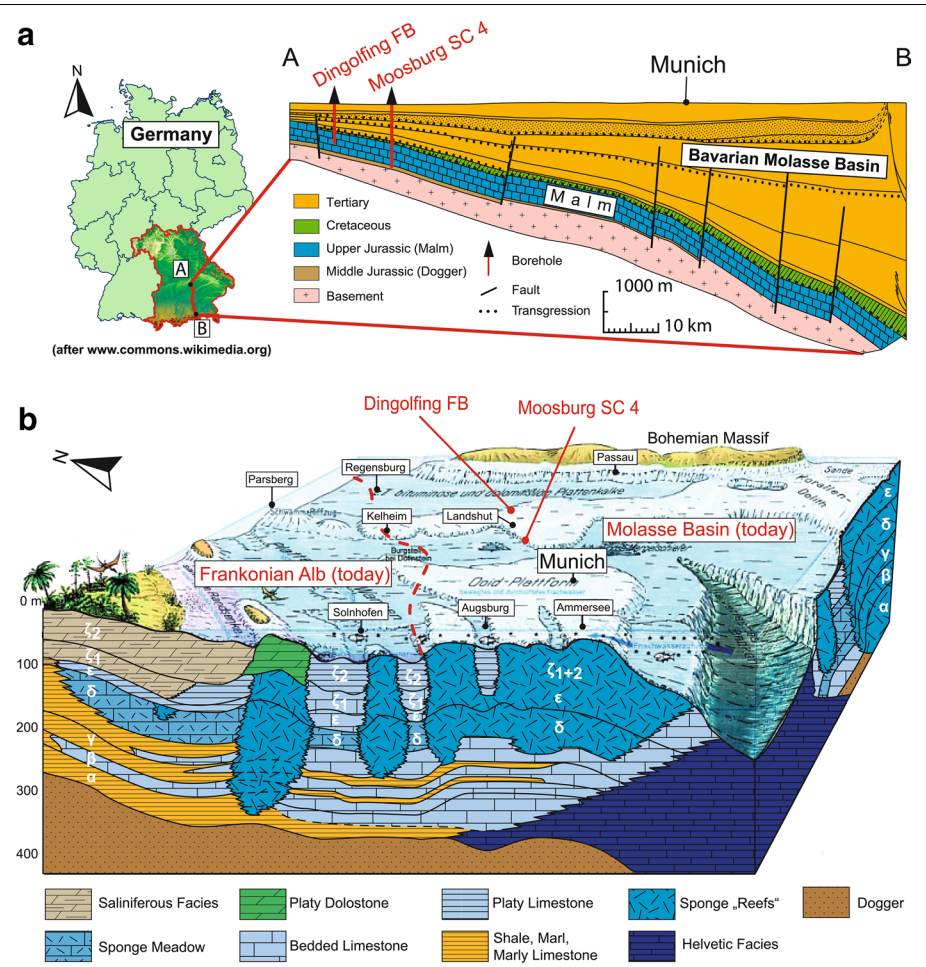

Fig. 1 Overview over the geological setting of the Jurassic sediments in South Germany. **a** Cross section through the South German Molasse Basin (from BayStMivt 2012; modified after Lemcke 1988). **b** Distribution of the calcareous Malm deposits during the uppermost Jurassic. Note the heterogeneity of depositional sequences due to local development of reefal buildups in alternation with restricted lagoons and small enclosed basins (modified after Meyer and Schmidt-Kaler 1990a)

Upper Jurassic carbonate deposits (Meyer and Schmidt-Kaler 1996). These carbonates in turn directly rest on Permo-Carboniferous troughs and a Variscan crystalline complex (Lemcke 1988). The Upper Jurassic is composed of alternating shallow marine sequences of limestones, marls, and dolostones that can be separated into a massive and a bedded facies (Meyer and Schmidt-Kaler 1990b) (Fig. 1b). The deposits can reach a thickness of up to 400 m, with the depth increasing south to about 5 km below the fringe of the Alps (Goldbrunner and Vasvári 2016; Mraz 2019).

As a result of the Alpine orogeny, the Molasse Basin is a typical wedge-shaped foreland basin formed by tectonic movements. The formation of synsedimentary fractures and fault zones is widespread throughout the southern part of the basin, directly influencing the carbonates of the Upper Jurassic (Bachmann et al. 1987; Büchi et al. 1965). In addition, the carbonate deposits were affected by emersion during the Cretaceous resulting in locally extensive erosion and karstification (Koschel 1991).

As a result of the high variability in its depositional environment (Fig. 1b), sedimentary and diagenetic features as well as irregular fractures, faults, and locally intensive karstification, the aquifer properties are very heterogeneous throughout the basin (Koch et al. 1994, 2010; Koch 1997, 2000; Koch and Munnecke 2016; Mraz 2019; Niebuhr 2014; Stier and Prestel 1991). Therefore, petrophysical and hydraulic properties of the aquifer rock are presumed to be variable throughout this carbonate platform setting as well. A detailed evaluation of pumping tests in the Munich area showed that, contrary to the expectation of a rather linear or bilinear flow, a significantly more frequent radial flow could be observed (Konrad et al. 2019). Most of the investigated geothermal boreholes (37 of 41) show a homogeneous flow behavior, which was observed by the interpretation of pressure derivatives and indicates radial flow conditions. Hence, these wells seem not to be entirely dominated by faulted, fractured, and karstified zones alone and benefit or are even masked by considerable volume produced from the rock matrix. For characterization of the reservoir, porosity and permeability of the rock matrix combined with fractures and karstified zones are controlling factors regarding the storage and flow of fluids. They have an impact on a variety of different rock properties like rock density, thermal conductivity as well as geomechanical parameters (Stober and Bucher 2013). For thermal, hydraulic, and mechanical modeling (THM) of a reservoir, the distribution and variety of these parameters for each type of rock are required as an important input parameter range (Brehme et al. 2016; Cacace and Jacquey 2017; Cherubini et al. 2013; Jacquey et al. 2018; Konrad et al. 2019). For a better prediction of mining models and productivity prognosis in the Molasse Basin, it is therefore necessary to investigate these parameters and their influence on local aquifer conditions in detail.

The heterogeneity of carbonate deposits on a regional scale causes difficulties in generalization and transferability of the measured properties (Eaton 2006; Koltermann and Gorelick 1996; Lucia et al. 1992). To improve the understanding of the regional distribution, the correlation of real aquifer parameters (from rock cores) with information from outcrops and geophysical borehole measurements is crucial. However, comprehensive geophysical logging in geothermal wells throughout the South German Molasse Basin is for many different reasons (e.g., costs, risks, technical problems) scarce, incomplete, or even missing. Additionally, rock cores of the aquifer section are usually not acquired during the geothermal exploration. Reliable petrophysical data for the characterization

of the aquifer is therefore based on literature, analogue outcrops, research wells (e.g., Moosburg SC4), or hydrocarbon wells. These outcrops are located some 100 km from the drilling sites of the central Molasse Basin and were subject to decompaction and weathering (Hedtmann and Alber 2017, 2018; Homuth 2014; Mraz et al. 2018). Hence, the representativity and transferability to reservoir conditions of these data are quite questionable.

To improve the understanding of the hydraulic, thermal, and geomechanical behavior of the aquifer rock matrix, several samples from two of those rare cored boreholes were investigated for laboratory experiments in this study. The cores of the exploration drillings Moosburg SC 4 and Dingolfing FB, which are located in the center of the Molasse Basin near a structural high ("Landshut-Neuöttinger Hoch") comprise a complete succession of the upper Jurassic sediments and shall therefore be used as a reference for correlation towards the center of the basin. The transferability of these data to other wells in the Molasse Basin based on the correlation with downhole logs is also exemplarily shown in this research.

Previous investigations in the Molasse Basin

Petrophysical rock characterization is a common practice in the field of reservoir engineering to describe hydraulic properties of an aquifer (Essley 2013; Okotie and Ikporo 2019). A few studies already described the petrophysical and hydraulic properties of the Upper Jurassic aquifer of the Bavarian Molasse Basin in the context of geothermal exploration. Most of these studies focused more on local areas or specific projects for which detailed data should be evaluated. A summary of most available data sets for porosity of the Upper Jurassic in comparison with the results of this research is shown in Appendix 1.

The hitherto most comprehensive work was carried out by Homuth (2014) and Homuth et al. (2014, 2015). The authors investigated petrophysical properties on several samples from outcrops and shallow boreholes of the Swabian and Franconian Alb, which represent an analogous area for the Malm aquifer. However, only very few selected samples of deep boreholes from the Malm reservoir were investigated (Moosburg SC 4, Geretsried GEN-1).

Mraz et al. (2018) used a similar approach to describe hydraulic, petro- and thermophysical properties of analogous outcrop material to transfer it to the deep geothermal well Geretsried GEN 1 ST. Effective porosities for gas and water were measured with a helium gas expansion porosimeter (HEP) and water immersion porosimetry (WIP). Analogous samples were taken from quarries and outcrops in the Southern Franconian Alb.

Hedtmann and Alber (2017, 2018) also investigated analogous material from the Southern Franconian Alb to collect petrophysical and hydraulic parameters for the Malm aquifer.

Böhm et al. (2010) analyzed hydraulic active zones of borehole Moosburg SC 4 by investigation of permeable and porous intervals. Measurement of effective porosity was realized on selected rock core samples by WIP and petrographic image analysis (PIA) of thin sections (total porosity). Permeability was measured for some samples in a Hassler type cell. At the geothermal well Pullach Th 2, Böhm et al. (2010) used PIA on thin

sections of drill cuttings to describe porosity for different stratigraphic intervals in the vicinity of Munich.

Beichel et al. (2014) developed a water saturation and vaporization method to allow the assessment of effective porosity for drill cutting samples from a drilling project in Unterhaching near Munich.

Nonetheless, the abovementioned studies focused primarily on analogous outcrop samples and drill cuttings of some boreholes. Only a few selected core samples of the buried reservoir were investigated for the characterization of porosity and permeability distribution. The common goals of these studies are the correlation of petrophysical properties from drill cutting/core or outcrop samples to different areas of the aquifer within the Molasse Basin. However, the high heterogeneity throughout the depositional sequences of the Upper Jurassic remains as the main problem for correlation of analogous outcrop data or selective core data to the whole aquifer system buried beneath the Molasse Basin.

To properly address this problem, a high quantity of rock samples from two almost-complete drill cores from the reservoir were examined in this study. Based on this data set, a detailed porosity and permeability distribution can be provided with respect to utilization as input parameters for models and simulations. Transferability of data to other locations in the Molasse Basin can be achieved by correlation with downhole logs of already existing and future drillings.

Materials and methods

Workflow

To improve the data basis for hydraulic and petrophysical properties of the reservoir, rock samples of drilling cores were investigated. After the acquisition of drilling cores, a description of lithology, facies, and microstructures was carried out before the cores were sampled and subsequently prepared for further procession in the laboratory workflow (Fig. 2). Rock density, effective porosity, and permeability were measured using different methods and saturation/flow media (water, air/gas). The obtained parameter set was then consolidated into distributions based on lithofacies and microstructural aspects in order to develop a statistical poro–perm relationship. As a result, an empirical permeability model based on lithofacies and porosity was developed. In addition to the laboratory workflow, the porosity was interpreted from an electrical resistivity log of a geothermal well. The calculation of the porosity following Archie's law was supplemented with parameters based on the laboratory results. The permeability was then estimated using different existing permeability models and validated by the empirical model based on laboratory results. Finally, local flow zones could be identified within the reservoir that can be correlated in a regional context.

Materials and preparation

In this study, two of the rare rock cores comprising the entire reservoir section of the Malm reservoir, Moosburg SC 4 (MSC-4) and Dingolfing FB (DGF-FB), were available for laboratory experiments on several rock samples.

The exploration well MSC-4 was drilled in 1990 to a total vertical depth of 1585 m (Fig. 3). The reservoir section (Upper Jurassic Malm Aquifer), which is capped by

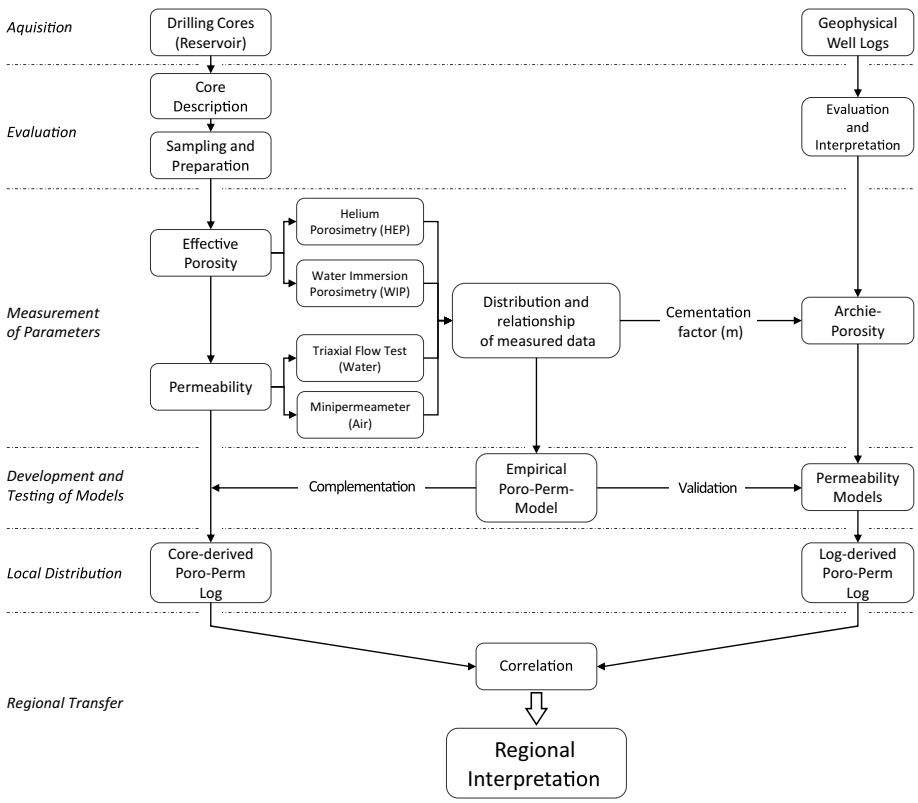

Fig. 2 Workflow for determination of hydraulic parameters from drilling cores and downhole logs

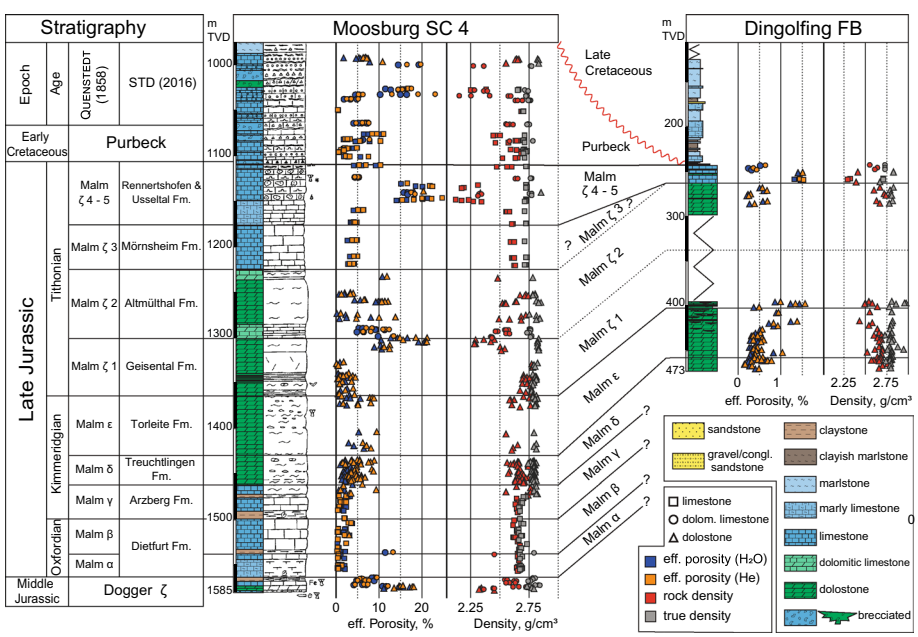

Fig. 3 Schematic correlation of the Upper Jurassic sections of the boreholes Moosburg SC 4 and Dingolfing FB. In addition to lithology, the porosity and density data measured during this research are shown. Each pair of values represents the location of a core sample in the corresponding depth (based on Meyer 1994)

deposits of the Purbeck and underlain by sediments of the Dogger, was cored completely over a total length of approximately 453 m (Böhm et al. 2011; Böhm 2012; Meyer 1994). The Purbeck and the top of the Dogger formations were also cored and investigated. The Malm is composed of an alternation of limestones, dolomitized limestones, and dolostones (Fig. 3). Limestone can be found in the top and bottom parts of the borehole, whereas the middle part predominantly consists of dolostone. Limestone as well as dolomite rocks vary in their appearance throughout the borehole and show changes in facies and crystal size of the crystalline dolostone. Furthermore, the significant influence of tectonic fracturing and karstification affected the aquifer in the vicinity of the borehole MSC-4 (Böhm et al. 2011).

The well DGF-FB was drilled in 2014 as part of an industrial research project for the storage of thermal energy in the reservoir (Ueckert and Baumann 2019). The well reached a total vertical depth of 473 m and intersected about 230 m of the Upper Jurassic Malm succession with a successful coring of 130 m in total. The aquifer section is mainly composed of crystalline dolomite rock with varying bedding and crystal size and capped by about 20 m of limestone deposits at the top (Fig. 3). However, compared to the complete Malm-sequence found in the borehole MSC-4 located about 50 km south-west, the borehole DGF-FB was not completely drilled down to the base of the Malm. Additionally, the succession seems to be incomplete at the top. Due to a local horst structure related to a local ridge ("Landshut-Neuöttinger Hoch"), the deposition in this area could have been affected already during the Upper Jurassic (BayGLA 1996). This may have resulted in reduced accommodation space and less deposition or even nondeposition during the latest depositional sequences of the Upper Jurassic or extensive erosion caused by temporary exposure of this area. Therefore, the correlation of the upper part of the succession to the section of the borehole MSC-4 is not entirely unambiguous. However, the middle part of the Malm shows a similar lithology for both boreholes to the maximum depth of the borehole DGF-FB.

A detailed description of lithology, facies, and rock fabric was accomplished for the entire rock core in order to assign the petrophysical measurements to different rock properties. Limestone and dolomitic limestone were subdivided into groups of different grain and particle/component size (Dunham 1978; Flügel and Munnecke 2010; Lucia 1995, 2007; Lucia and Conti 1987). Dolostone was classified with regard to dolomite crystal size into three major groups: fine, medium, and coarsely crystalline (Beichel et al. 2014; Folk 1974; Lucia 2007; Sibley and Gregg 1987). Morphology of dolomite crystals was also taken into account ranging from irregular to well-shaped dolomite rhombs (xenomorphic, hypidiomorphic, idiomorphic) (Sibley 1982; Sibley and Gregg 1987; Tucker and Wright 1990).

In order to ensure a representative data set for the whole reservoir, samples were taken according to changing stratigraphic intervals as well as varying lithology and facies alongside the rock cores. However, the sample intervals had to be adjusted to the quality of core recovery and the local occurrence of core disking and fragmentation. Test plugs with a diameter of 50 mm were drilled from the original rock core parallel to its vertical axis. The plugs were then cut to a standard length of 100 mm and ground for smooth and perpendicular end faces to achieve best possible cylindrical test specimens according to the ASTM Standard D4543-08e1 (2008). Following this procedure, a total

of 363 test plugs of the rock cores MSC-4 and DGF-FB were prepared and subsequently analyzed. The effective porosity was measured for all 363 samples by two different techniques using purified water (WIP) or helium (HEP) as saturation fluid (Table 1). Additionally, the permeability for 65 of these samples was measured. Most of the test plugs (40) met the requirements for measurement in the triaxial test cell (minimum length of 90 mm, no vugs and cavities connected to sample surface). However, 25 test plugs had to be measured with an air-driven minipermeameter to cover parameter ranges for desired stratigraphic units, lithologies or facies types that could not be measured by the triaxial flow test.

Experimental techniques

Porosity

The effective porosity ϕ_{eff} is defined as fraction of the interconnected nonsolid volume allowing flow through the rock and is described as a percentage (%) in this research. To allow a comparison and evaluation of results from different measurement techniques or rock types, porosity deviations are referred to as absolute difference $\Delta\phi_{\text{eff}}$ in % p.u. (porosity unit) (Schlumberger Oilfield Glossary 2018).

Helium porosimetry (HEP) The gas expansion method is seen as one of the most accurate and repeatable non-destructive techniques for determination of effective porosity in a variety of rock types (Anovitz and Cole 2015; McPhee et al. 2015). In order to quantify the porosity of a rock sample using HEP, several different steps of preparation and measurement must be performed. For calculation of $\Delta\phi_{\text{eff}}$, the specific volumes of the sample have to be measured. Those are the bulk volume V_{b} and the grain volume V_{g}, which describe the total volume or rather the pure volume of grain material excluding

Table 1 Overview of rock samples and the corresponding measurement methods

Location	Stratigraphy	Porosimetry			Permeability		
		HEP	WIP	Total	AirPerm	Triax	Total
Moosburg SC 4	Purbeck	73	73	73	5	2	7
	Malm ζ 4–5	32	32	32	5	3	8
	Malm ζ 3	18	18	18			
	Malm ζ 2	35	35	35	2		2
	Malm ζ 1	32	32	32	5	2	7
	Malm ε	19	19	19	4	1	5
	Malm δ	36	36	36	4		4
	Malm γ	15	15	15			
	Malm β	14	14	14			
	Malm α	18	18	18			
	Top Dogger	20	20	20			
Dingolfing FB	Malm ζ 4–5	6	6	6		3	3
	Malm ζ 2	9	9	9		7	7
	Malm ζ 1	5	5	5		3	3
	Malm ε	19	19	19		13	13
	Malm δ	12	12	12		6	6
Total		363	363	363	25	40	65

HEP helium porosimetry, *WIP* water immersion porosimetry, *AirPerm* minipermeameter, *Triax* triaxial flow test

pores. Usually bulk volume of a sample can be determined by buoyancy methods based on the principle of Archimedes (American Petroleum Institute 1998). Bulk volume V_b (1) was therefore calculated by measurement of sample dimensions at several points using a digital caliper (height L= mean of 8 readings, diameter u = mean of 6 readings) to ensure the best possible accuracy. Dry sample weight W_d was collected by repeated weighing ($\geq$ 5 times) with accuracy of 0.01 g (McPhee et al. 2015) so that bulk density ρ_b (2) can be calculated:

$$V_b = \pi \cdot \left(\frac{u}{2}\right)^2 \cdot L, \tag{1}$$

$$\rho_b = \frac{W_d}{V_b}. \tag{2}$$

A helium pycnometer with accuracy within ± 0.03% and reproducibility within ± 0.02% was used to measure the pore volume, effective porosity, and grain density (Micromeritics, AccuPyc II 1340 Series). Following Boyle's law, the required parameters can be determined by displacement of known volumes of injected gas. Helium of high purity is used due to its inert character that minimizes the absorption of gas on the core surface and therefore the influencing of the measurement. The helium grain volume V_g^{He} of the rock sample is the direct output of this method. However, some isolated pores may affect measurement of V_g^{He} as they cannot be penetrated by gas. The connected pore volume V_P^{He} (3), grain density ρ_g (4) and effective porosity ϕ_{eff}^{He} (5) can be calculated as following:

$$V_P^{He} = V_b - V_g^{He}, \tag{3}$$

$$\rho_g = \frac{W_d}{V_g^{He}}, \tag{4}$$

$$\phi_{eff}^{He} = \left(1 - \frac{V_g^{He}}{V_b}\right) * 100\%. \tag{5}$$

Water immersion porosimetry (WIP) The Water Immersion Porosimetry (WIP) was used to determine the effective porosity of rock samples for the fluid water. The method is based on imbibition of purified water by immersion of the rock sample under vacuum. Before saturation, the sample was oven dried at 105 °C for 48 h and the weight of the dry sample W_d was measured. Subsequently, the sample was placed in a desiccator under vacuum to remove trapped air/gas from connected pores. The desiccator was then flushed with purified water until the rock sample was completely covered. Vacuum was maintained for at least 72 h to ensure best possible saturation before saturated weight W_s^w of the sample was measured. Assuming a known constant density of the imbibed water ρ_w (0.997 g/cm^3 at 24–26 °C) (Wagner and Pruß 2002), the pore volume V_P^w (6) and effective porosity ϕ_{eff}^w (7) can be calculated (American Petroleum Institute 1998; Anovitz and Cole 2015; McPhee et al. 2015):

$$V_{\mathrm{P}}^{\mathrm{w}} = \frac{\left(W_{\mathrm{s}}^{\mathrm{w}} - W_{\mathrm{d}}\right)}{\rho_{\mathrm{w}}}, \tag{6}$$

$$\phi_{\mathrm{eff}}^{\mathrm{w}} = \frac{V_{\mathrm{P}}^{\mathrm{w}}}{V_{\mathrm{b}}} \cdot 100\%. \tag{7}$$

Porosity from log interpretation (Archie-porosity) For correlation and validation of the measured porosity data, porosity of a geothermal well near Munich using the deep electric resistivity reading of a downhole log was calculated by Eq. (8) proposed by Archie (1942):

$$R_0 = R_{\mathrm{w}}\phi^{-m}, \tag{8}$$

where R_0 is the resistivity of 100% water-saturated rock, R_{w} is resistivity of the formation water, ϕ is the fractional porosity of the rock matrix and m is the cementation factor.

The lithology and facies of the aquifer were interpreted by cutting samples (mud log) and downhole logs (Gamma, Image) and processed in the software "Interactive Petrophysics" (IP). For calculation of porosity from resistivity logs, knowledge of formation water resistance R_{w} and cementation factor m are required. R_{w} was determined from the hydrochemical analysis of formation water which generally shows low mineralization throughout the Malm of the central Molasse Basin (Birner et al. 2011; Stober et al. 2014). The m value depends on the rock fabrics and is mainly subject to vuggy porosity in carbonate rocks (Lucia and Conti 1987). The cementation factor for this carbonate reservoir has not yet been determined and therefore had to be estimated. Lucia (2007) suggested to use $m = 2$ for heterogeneous carbonate deposits as usually applied in the hydrocarbon industry, while Rashid et al. (2015) recommended a range of $2 < m < 4$ for well-cemented carbonates. However, knowing the effective porosity (interparticle porosity) and permeability from laboratory measurements, the cementation factor can also be determined by empirical power laws to validate the abovementioned assumption and assign m values to different lithology and facies. Following Focke and Munn (1987), the uncertainty in estimating the cementation factor can be considerably reduced by the following trends for carbonate core samples:

$$m = 1.2 + 0.1286\phi_{\mathrm{eff}} \quad \text{for } k < 0.1 \text{ mD}, \tag{9}$$

$$m = 1.4 + 0.0857\phi_{\mathrm{eff}} \quad \text{for } k \geq 0.1 \text{ mD} < 1 \text{ mD}, \tag{10}$$

$$m = 1.2 + 0.0829\phi_{\mathrm{eff}} \quad \text{for } k \geq 1 \text{ mD} < 100 \text{ mD}, \tag{11}$$

$$m = 1.22 + 0.034\phi_{\mathrm{eff}} \quad \text{for } k \geq 100 \text{ mD}, \tag{12}$$

where m is the lithology component or cementation factor, k is permeability in millidarcy (mD), and ϕ_{eff} is effective or interparticle porosity (%).

A rather simple approach to calculate the m value was suggested by Borai (1987) in form of an empirical cementation factor versus porosity relation found for a wide range of porosities for pure limestones offshore Abu Dhabi:

$$m = 2.2 - 0.035/(\phi + 0.042). \tag{13}$$

The relationship of Focke and Munn (1987) was used for 61 samples with both known porosity and permeability while that of Borai (1987) was used for 298 samples where only porosity data are available.

Limitations of the Archie-approach can be the changes in mineralogy and the occurrence of borehole breakouts and karstification. Due to the increasing clay content from the section Malm γ to Malm α the simple Archie equation could not be used without correction (Waxman and Smits 1968). Accordingly, the log porosity was calculated based on the Archie equation only for the Purbeck and the sections Malm ζ–δ, which corresponds to the total depth of the well near Munich. Open fractures with opening widths of maximal 0.1 mm at a fracture spacing of at least 10 cm throughout the aquifer were determined from the Image log of the same well. According to Lucia (1983), this corresponds to a fracture porosity of less than 0.1% and was therefore neglected for calculation of log porosity. Furthermore, log porosity can be affected by breakouts and zones showing abundant vugs or karstification. These zones were detected by interpretation of the Caliber and Image logs and highlighted accordingly (compare "Scale of observation and transfer of parameters for regional interpretation" section).

Permeability

Identification of permeability is of major importance to identify productive flow zones in a geothermal aquifer (Mahjour et al. 2016). Permeability is a rock property that is directly linked to pore size and effective porosity and varies widely in heterogeneous carbonate deposits from < 0.01 millidarcy (mD) to well over 1 Darcy (Lucia 2007). Therefore, core samples from different types of lithology and facies of the aquifer were selected to determine ranges for each type and heterogeneity within the aquifer. Permeability was measured for 65 core samples by two different techniques using water and air as fluid (Table 1). Based on the poro–perm relationship of the measured core samples, permeability was also calculated using different empirical power laws and models to estimate the permeability of the entire aquifer section based on the derived porosity distribution.

Triaxial flow test—water permeability To determine the permeability by the triaxial cell, the percolation of deionized water was tested for 40 cylindrical core samples under hydrostatic conditions (Fig. 4a). After the core sample was installed in the sample holder of the test cell, a vacuum was applied and the sample was saturated from bottom to top against a closed downstream fluid port until the pore pressure was constant. The sample was then flushed for several hours with the downstream reservoir open to atmosphere to remove trapped air from the sample. Following saturation of the core sample, axial and confining stress were cycled up to 30 MPa to eliminate inelastic behavior and to close microcracks that may have resulted during decompaction of the rock core. For permeability measurements, hydrostatic stress was maintained at 3 MPa with a fixed flow rate of $Q_{up} = 0.15$ ml/min at the upstream fluid port resulting in pore pressures between 1.0 and 1.5 MPa. After reaching stationary flow between up- and downstream pump ($Q_{up} = Q_{down}$) and stabilization of pore pressure, flow through the sample was measured over a period of at least 6 h for time steps of 5 min. Temperature of the fluid and at the

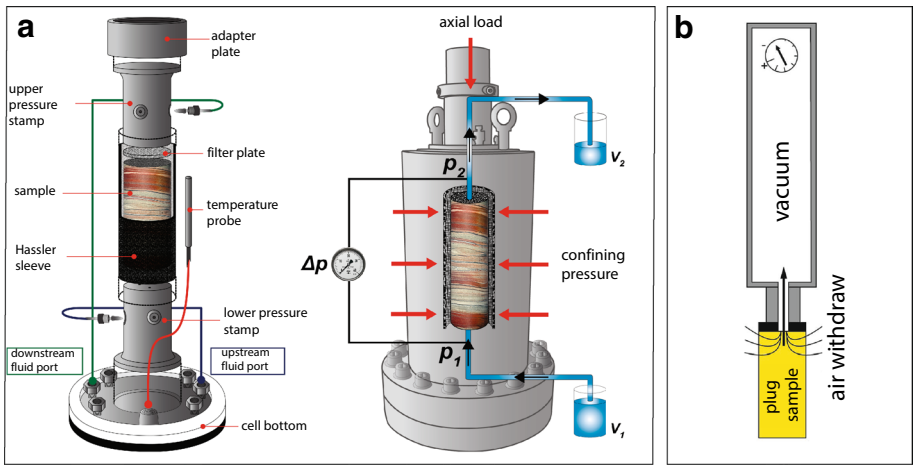

Fig. 4 Test design for permeability measurement on cylindrical core samples. **a** The core sample is placed between axial pressure stamps and connected to pore fluid pressure pumps establishing vertical flow. The sample is jacketed by a Hassler sleeve in order to separate pore and confining pressure. **b** Tiny Perm II minipermeameter to determine permeability by applying a vacuum (modified from Filomena et al. 2014)

sample were recorded during the test for correct determination of fluid properties. Permeability was calculated according to Darcy's Law (Darcy 1856; Lucia 2007) (14):

$$k = \left(\frac{Q_{\mathrm{av}} * \mu * L}{A * \Delta P_{\mathrm{p}}} \right), \tag{14}$$

where Q_{av} is the averaged flow between up- and downstream ports (in $\frac{m^3}{s}$), k is the permeability (in m^2), μ is the dynamic viscosity of the fluid (in $\mathrm{Pa} \cdot \mathrm{s}$) as a function of measured temperature, ΔP_{p} is the pore pressure drop (in Pa) across the length of the sample L (in m) and A is the cross-sectional area of the sample (in m^2). The permeability was converted to the unit millidarcy (mD) using Eq. (15), which is commonly used to evaluate the hydraulics of reservoir rocks:

$$1\mathrm{mD} = 9.86923 \cdot 10^{-16}\ \mathrm{m}^2, \tag{15}$$

Minipermeameter—air permeability For measurement of air permeability, the "Tiny Perm II", a portable probe minipermeameter designed by *New England Research Inc.* for measurements of air-driven permeability, was used. The measurement is performed by pressing a nozzle with rubber seal against the rock surface connected to a vacuum test chamber (Fig. 4b). The vacuum dissipates by flow of air through the rock matrix while volume and time are recorded by a microcontroller and computed to a device-specific value (T). The permeability can subsequently be calculated through a specific conversion equation provided by the manufacturer (16):

$$T = -0.8206 \cdot log_{10}\left(k_{\mathrm{g}}\right) + 12.8737, \tag{16}$$

where T is a device-specific value without unit and k_{g} is the air permeability in millidarcy (mD).

Filomena et al. (2014) provide a specific description of test design, procedure, and limits of the test device. In order to obtain resilient values, several measurements per sample were carried out and combined to a mean value. Air permeability was successfully tested on 25 cylindrical core samples of different lithology and facies. According to Filomena et al. (2014), the measured permeability results have to be reduced by 37% to correct for shorter flow paths, resulting in apparently higher permeabilities for plug samples compared to field measurements.

In addition, since permeability as an intrinsic rock parameter is independent of fluid properties, a correction is required for a direct comparison of air and water-derived permeabilities due to non-Darcy flow (McPhee et al. 2015, Tanikawa and Shimamoto 2006). In a low-pressure gas flow through a porous medium, the mean free path of gas molecules approaches the size of the pores and individual molecules can accelerate due to interaction with the pore walls (Bear 2013; Klinkenberg 1941; McPhee et al. 2015). The laminar flow theory of Darcy's law is not valid under these conditions, which results in higher flow velocities and permeability results (Bear 2013; McPhee et al. 2015). According to Filomena et al. (2014), gas permeabilities of sandstone tend to be about 50% higher than those derived with water. Accordingly, the carbonate samples measured in this work showed distinctly higher deviations even after the correction by 37%.

Air permeability was therefore measured at several points on the end faces of some sample plugs, which were also measured for water permeability, in order to find a suitable correction factor. By correlation and fitting of data points, a correction was found by the following relationship (17):

$$K_{\mathrm{i}} = 0.94 \cdot (k_{\mathrm{g}} \cdot 0.63) - 0.09, \tag{17}$$

where K_{i} is the intrinsic permeability in mD, k_{g} is the gas permeability in mD, and the value 0.63 corresponds to the correction factor after Filomena et al. 2014.

Permeability models Since the availability of rock cores for direct measurement of permeability is generally scarce and permeability cannot be derived directly from available geophysical downhole logs (Lucia 2007), an estimation of permeability using existing parameters is necessary. The quantification of permeability for a porous medium has already been attempted by several authors, who estimated permeability based on different properties of the porous rock material, such as characteristic grain size, pore geometry or porosity (Glover et al. 2006; Hommel et al. 2018; Nelson 1994). Many of the permeability models are based on the modification of the Kozeny–Carman relationship, which describes the flow in a porous medium through a tubular pore model as a function of the pressure drop when flowing through tubes of different shapes and radii (Carman 1937; Kozeny 1927).

In this study, various empirical laws (e.g., power laws) based on the measured effective porosity as a function of the rock properties (facies, grain size, cementation factor) were used to assess the permeability of the aquifer. By establishing the global porosity–permeability transform (GPPT) (18), Lucia et al. (2001) and Jennings and Lucia (2003) used a similar approach by assigning a *rock fabric number (*rfn*)* (0.5–4.0) for petrophysical classes. Mud-supported limestones and fine crystalline dolostones are assigned a rfn of $4.0 - 3.5$, grain-supported packstone and medium crystalline dolostones refer to a rfn

of 2.5 − 1.5, and grainstones and coarsely crystalline dolostones to a rfn of 1.5 − 0.5. Permeability can be calculated based on porosity data for each petrophysical class by the use of multiple linear regressions:

$$\log(k) = \left(A - B \cdot \log(\mathrm{rfn})\right) + \left(\left(C - D \cdot \log(\mathrm{rfn})\right) \cdot \log\left(\phi_{\mathrm{ip}}\right)\right), \tag{18}$$

where k is permeability of the rock, $A = 9.7982$, $B = 12.0838$, $C = 8.6711$, $D = 8.2965$, rfn is the rock fabric number (0.5–4), and ϕ_{ip} is the fractional interparticle porosity (effective porosity).

The GPPT was also used for the data set of this study to compare it to empirical power laws for each petrophysical class of the core samples. The rock fabric numbers used for calibration of the GPPT model are listed in Table 2.

In clastic reservoirs permeability can also be calculated as a function of the geometric mean grain diameter. Berg (1970) discovered a complex relationship of permeability with grain packing, grain size, grain sorting, and porosity calibrated with empirical data of a sandstone reservoir. The Berg model (19) was simplified using only the mean grain size (Berg 1975; Glover et al. 2006) and can therefore also be used for estimation of permeability in carbonate rocks replacing grain size by mean particle size:

$$k_{\mathrm{B}} = 8.4 * 10^{-2} \mathrm{mp}^2 \phi^{5.1}, \tag{19}$$

where k_B is permeability in m^2, mp the mean particle size in m. The mean particle size used for calibration of the Berg model is listed in Table 2.

Glover et al. (2006) introduced another model for permeability prediction (RGPZ model) (20) based on electrokinetic coupling between fluid flow and electrical flow in a porous medium. The permeability can be calculated using the RGPZ model by:

$$k_{\mathrm{RGPZ}} = \frac{d^2 \phi^{3m}}{4am^2}, \tag{20}$$

where k_{RGPZ} is the permeability in m^2, d is the geometric mean grain size in m, a is the packing parameter, and m is the cementation factor.

Table 2 Calibration data for permeability models GPPT and Berg model for different facies types

Lithology	Facies	rfn	mp (d) [m]
(Dolomitic) limestone	Mudstone	4	$3.0 * 10^{-5}$
	Wackestone	4	$3.0 * 10^{-5}$
	Packstone (grain-supported)	4 (3)	$3.0 * 10^{-5}$
	Grainstone	1.75	$1.25 * 10^{-4}$
	Rud/floatstone	1.5	$5.0 * 10^{-4}$
Dolostone	Fine crystalline	3.5	$6.3 * 10^{-5}$
	Fine–medium crystalline	3	$2.2 * 10^{-4}$
	Medium crystalline	2.5	$3.5 * 10^{-4}$
	Medium–coarsely crystalline	2	$4.0 * 10^{-4}$
	Coarsely crystalline	1.5	$5.0 * 10^{-4}$

Rfn rock fabric number, *mp* mean particle size, *d* geometric mean grain size

The RGPZ model was used for all measured samples to compare it to the empirical based permeability models. Mean grain size was replaced by mean particle/crystal size and determined for every petrographic group by evaluation of core samples and thin sections. The geometric mean grain size used to calibrate the RGPZ model is shown in Table 2, while the packing parameter was set to $a = 8/3$, as proposed by Glover et al. (2006) and Rashid et al. (2015). The model was tested with both approaches of Borai (1987) and Focke and Munn (1987) to estimate the cementation factor as described in "Porosity" section.

Results and discussion

Effective porosity

The result of all investigations is a wide-ranging data set of porosity values comprising different methods and various sample properties. The porosity data must therefore be classified under specific aspects to make the results valuable for input parameters in models and for a regionalized reservoir characterization to improve the prediction of production rates. Accordingly, the measured porosity data have to be subdivided into different groups defined by measurement method, sample location, stratigraphy, lithology, and facies or secondary processes like dolomite crystal size. Each class was evaluated regarding its statistical distribution and correlated with classes of other groups to gather information about direct relationships in the superordinate context of the aquifer system.

Due to the rather complex pore space geometry and surface roughness of the carbonate matrix, which is already heterogeneous on a small scale, the saturation of the core plugs with fluids can be influenced by wettability of the rock matrix (Arif et al. 2020). The porosity measured by saturation with the inert gas helium (HEP) is unaffected by wettability and represents the maximum effective porosity. On the contrary, the porosity measured by saturation with purified water (WIP) can be underestimated to an uncertain extent due to wettability and is therefore referred to as minimal effective porosity. In this study, a conservative approach was chosen to interpret the hydraulic properties of the rock matrix, using the minimum possible effective porosity to avoid an overestimation of the hydraulic properties. Consequently, the effective porosities from the WIP were used. A detailed comparison between HEP and WIP methods with possible deviation of effective porosity is provided in Appendix 2.

Subset stratigraphy

The compiled data set was subdivided according to the stratigraphic position in the Upper Jurassic succession of the Bavarian Molasse Basin. To better compare the data with reports of older drillings and data from the literature, the outdated subdivision of Quenstedt and Richter (1987) was used to describe the local strata. However, the recent classification of stratigraphy of the Upper Jurassic following the Stratigraphic Commission of Germany (STD 2016) is also provided in Appendix 1 and Fig. 3 (Menning and Hendrich 2016).

Appendix 3 shows the complete porosity data set classified to stratigraphy for the locations MSC-4 and DGF-FB. Besides porosity, the data set also includes information about the rock density and grain density of the rock matrix, which were obtained during the

experiments as well. The data set points out differences of porosity distribution due to stratigraphic interval and location of sample material.

Based on $\phi_{\mathrm{eff}}^{\mathrm{w}}$ data, the Upper Jurassic aquifer can be divided into three superior porosity units: Malm ζ, Malm ε–δ, and Malm α–γ (Fig. 5), agreeing with the interpretation of Böhm et al. (2013). The first unit shows high variety for the porosity of Malm ζ 1–5 with a range from 0.3 to 19.2% (median 4.8%) for both locations MSC-4 and DGF-FB. The distribution of porosity also shows a bimodal distribution for some of the units reflecting high variations in lithology and facies, as indicated by divergent average and median values (Fig. 5). However, the porosity in unit Malm ζ 3 seems to be more evenly distributed due to a more uniform lithology and facies based on the core description. Due to the fact, that no rock cores were extracted from the DGF-FB well in this section, this interval could only be evaluated at MSC-4 well. The second superior unit (Malm ε–δ) ranges between 0.5 and 12.2% (median 2.9%) and shows a rather unimodal distribution.

The outliers in unit Malm ε and Malm δ represent brecciated dolostones and dolostone containing abundant vugs. Apart from one strongly dolomitized sample with relatively high porosity (10.3%) which was identified as a statistical outlier for this unit, units Malm α–γ indicate a comparatively low and unimodal distribution of 0.3–3.5% (median 1.7%) and represent the third unit with the lowest porosity.

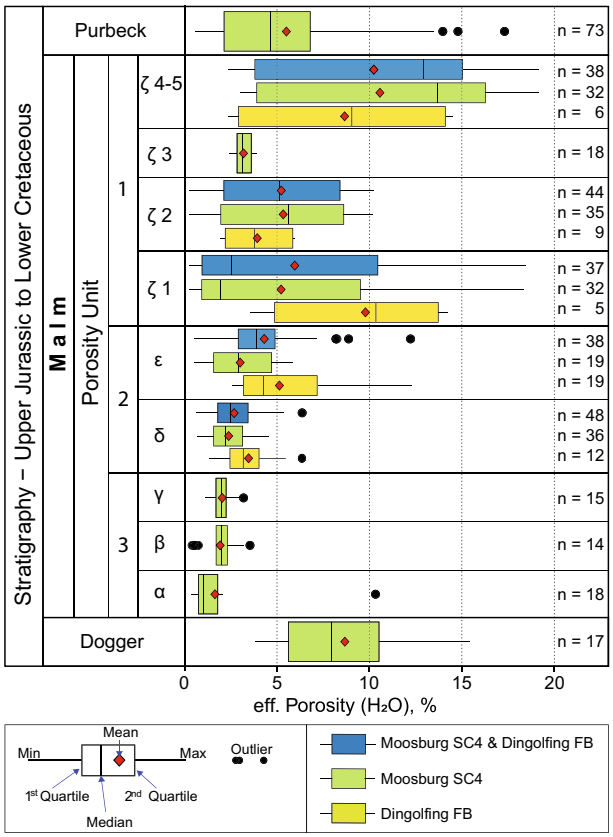

Fig. 5 Boxplots show the distribution of porosity for different stratigraphic Malm units and the classification into superior porosity units. The median porosity for most of the units seems rather low with unimodal distribution. Units Malm ζ 1, ζ 2, and ζ 4–5 overall show higher porosity values and a more bimodal distribution due to the heterogeneity of lithology and facies

The Upper Jurassic aquifer with its three porosity units is surrounded by the underlying Dogger and the deposits of the Purbeck capping the aquifer. The Dogger shows porosities ranging from 3.8 to 15.4% with a relatively high median of 7.9% compared to those of the Malm units. The Purbeck is characterized by a widespread bimodal distribution from 0.5 to 17.3% with a median of 4.6% and some outliers showing higher porosity values caused by increased interparticle porosity due to dolomitized in grainstones formed of black pebbles. Reasons for the high porosity variations are changing lithologies depending on the facies and the degree of dolomitization due to the regional heterogeneity of the depositional system and diagenesis. Figure 6 gives an example of how dolomitization affects rock density and porosity for samples from Malm ζ 4–5 of the same primary lithology and facies. Most units with a high variance in their porosity distribution also show a high variance in particle density (Appendix 3). This points to a variable lithological character within the unit.

Comparing the results of the drillings MSC-4 with DGF-FB regarding stratigraphic units, the distribution for some of the sections seems to be slightly different. Whereas $\phi_{\mathrm{eff}}^{\mathrm{w}}$ of Malm ζ 4–5 and Malm ζ 2 shows a lower median at DGF-FB, it was found to be higher for the units Malm ζ 1, Malm ε and Malm δ (Appendix 3). The high heterogeneity of the upper Malm units together with overall fewer available data from samples could affect the distribution for Malm ζ 4–5 to Malm ζ 2 and be the reason for the variety between both locations. For unit Malm ζ 1 only a few samples of the lowermost meters from the well DGF-FB could be investigated. The rock core shows partly intense brecciation accompanied by intense dolomitization and abundant intercrystal and vuggy porosity (Fig. 7e), which explains the high porosity of these samples. The rock core of MSC-4 also shows brecciated intervals at the basal part of this unit, but lacks the abundance of intercrystal and vuggy porosity compared to DGF-FB. The deviation for Malm ε can be explained by the fact that rock cores from the drilling MSC-4 showing abundant vuggy porosity in this unit, are often fragmented by intense core disking and could therefore not be included in the laboratory program. Hence, it can be assumed that the porosity distribution of the MSC-4 borehole could generally be higher in this interval and would rather correspond to the distribution of the DGF-FB borehole. For the Malm δ unit, the porosity distribution in both wells is quite similar and unimodal, although slightly higher

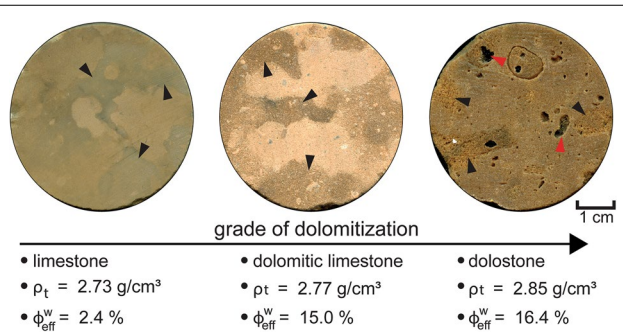

Fig. 6 Bioturbated wackestones showing different stages of dolomitization. Porosity increases with grade of dolomitization. Note bioturbation and burrows (black arrows) that are progressively substituted by sucrose dolomite rhombs. Location of the right sample is only 30 cm deeper than the middle one, but shows complete dolomitization with abundant intercrystal porosity and moldic porosity (red arrows). Left: DGF-FB, 246 mTVD, middle: MSC-4, 1138.9 mTVD, right: MSC-4 1139.2, mTVD

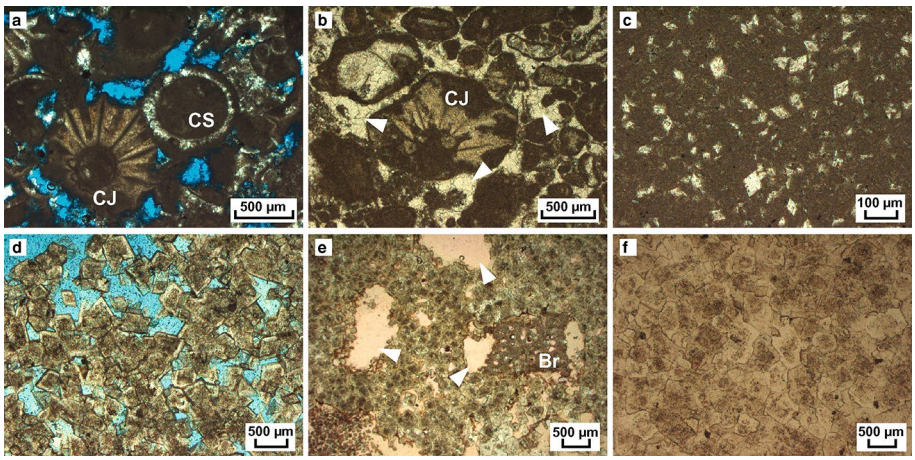

Fig. 7 Thin sections of Jurassic carbonate rocks from the Dingolfing FB rock core. **a** Fossiliferous grainstone of Malm ζ 4–5 section containing peloids and abundant fragments of green algae *Clypeina jurassica* (CJ) and *Campbelliella striata* (CS). Note interparticle porosity (blue staining) cumulating to $\phi_{\mathrm{eff}}^{\mathrm{w}}$ of 13.0% for the whole sample. **b** Same rock type and strata than in **a** but pore space is reduced by sparitic cementation (arrows) between particles. ($\phi_{\mathrm{eff}}^{\mathrm{w}} = 1.7\%$). **c** Euhedral dolomite crystals floating almost isolated in a microcrystalline calcite matrix of a dolomitic wackestone (Malm ζ 4–5). No porosity is visible in this thin section but $\phi_{\mathrm{eff}}^{\mathrm{w}}$ of sample is 2.4%. **d** Idiotopic dolostone (medium crystalline) with abundant intercrystal porosity (Malm ζ 4–5) reaching $\phi_{\mathrm{eff}}^{\mathrm{w}}$ of 16.3%. **e** Hypidiotopic dolostone (medium crystalline) showing some intercrystal and vuggy porosity (arrows) of dissolved fossil fragments. Fragment of a bryozoan (Br) is still preserved in one of the vugs ($\phi_{\mathrm{eff}}^{\mathrm{w}} = 8.6\%$, Malm ζ 1). **f** Xenotopic (non-rhombic) dolostone with sutures along contacts of coarse dolomite crystals (Malm δ). Due to complete dolomitization and compaction, pore space is highly reduced in this sample ($\phi_{\mathrm{eff}}^{\mathrm{w}} = 1.4\%$)

in the DGF-FB well, which may be related to a more frequent occurrence of vugs in this well.

As the classification solely by stratigraphic units is too unspecific for this heterogeneous aquifer, another more representative classification is needed to transfer porosity data to other boreholes or locations.

Subset lithology

To find more specific porosity patterns, the data set was additionally subdivided according to the lithology. Three major lithological groups were identified in both drillings—limestone, dolomitic limestone and dolostone. The distribution of $\phi_{\mathrm{eff}}^{\mathrm{w}}$ for limestone ranges widely from 0.4 to 19.2% with a median of 2.3%. The samples of dolomitic limestone show a slightly tighter distribution between 1.8 and 17.3% but a higher median of 6.1%, whereas porosity of the dolostone group ranges from 0.3 to 18.4% with a median of 3.1%. A comparison of porosity distributions according to lithology is presented in form of statistical box plots and histograms (Fig. 8a). When comparing the wells MSC-4 and DGF-FB, partially large deviations can be detected for lithology dependent porosity (Appendix 4). The median for $\phi_{\mathrm{eff}}^{\mathrm{w}}$ measured at DGF-FB is 11.6% p.u. higher for limestone but 3.3% p.u. lower for dolomitic limestone than that of MSC-4. Due to the missing or reduced strata of the upper part of the Malm of the borehole DGF-FB, only a small number of samples for the group limestone ($n = 2$) and dolomitic limestone ($n = 3$) could be measured. The greater variance in porosity may therefore be related to the lack of data. Nevertheless, the difference for dolostone shows only minor deviation of 1.4% p.u.

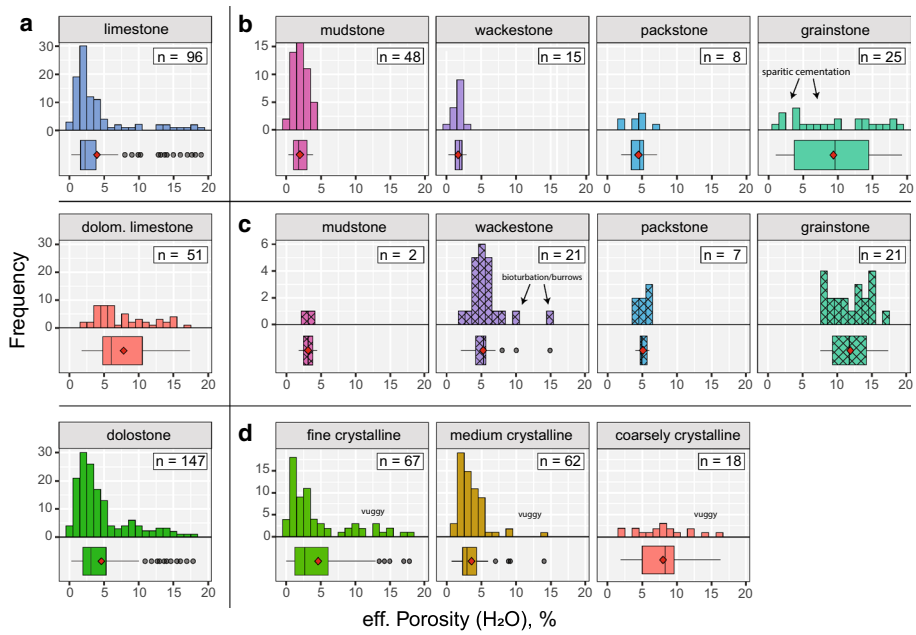

Fig. 8 Porosity distribution within different lithology and facies groups. **a** Data set subdivided by lithology shows a rather skewed distribution for each group. **b** Grouping by facies for limestone results in rather unimodal distribution for each type. Arrows point to reduced porosity due to sparitic cementation of pore space between particles in grainstones. **c** Facies groups of dolomitic limestone show a unimodal distribution of porosity, with exception of the grainstone group, which is more bimodally distributed. Some samples of dolomitic wackestone show abnormal high porosity due to intense bioturbation and dolomitized burrows. **d** Distribution of dolostone, grouped by crystal size, is still skewed in the fine and medium crystalline groups. Porosity is mainly controlled by crystal morphology and secondary porosity (vugs), which increases porosity

and is based on a larger dataset ($n = 45$). The upper part of unit Malm ζ 1 of the borehole MSC-4 consists of fine crystalline dolostone with relatively high porosity (1303–1316 m, $\phi_{\mathrm{eff}}^{\mathrm{w}} = 8.1$–$18.5\%$) (Fig. 3).

However, the separation of data solely by lithology still reflects insufficiently widespread porosity distributions, which might result in a high uncertainty when transferring ranges to other locations.

Subset facies, crystal size and morphology

The results for samples classified by facies, crystal size, and morphology show an apparent correlation of particle size with effective porosity, as it increases with coarsening of particles (Fig. 8, Appendix 5). For limestone samples of the group mudstone $\phi_{\mathrm{eff}}^{\mathrm{w}}$ ranges from 0.4 to 3.9% with a median of 1.8%. The group wackestone shows a rather similar distribution of 0.3–2.9% with a median of 1.9%. According to the increase in particle size, the groups packstone and grainstone show higher porosity values. The distribution for packstone varies between 2.1 and 7.1% with a median of 4.6%. The highest porosity values, but also widest spread are observed for the group grainstone. The porosity ranges from 1.1 to 19.2% with a median of 9.5% here. The wide spread is caused by samples showing abundant open pore space between particles with high porosity as well as samples where pores were almost completely filled by sparitic cement resulting in lower porosity values (Figs. 7a, b, 8b). By separating the group according to the occurrence

of sparitic cementation, the median for sparitic cemented grainstone would be 5.2% ($n = 12$) and 14.2% (8.9–19.2%, $n = 13$) for uncemented grainstone.

Overall, the results for the groups of limestone and dolomitic limestone show a similar relationship regarding grain size. However, effective porosity is usually higher for dolomitic limestone due to intercrystalline and interparticle porosity resulting from partial dolomitization (Fig. 6) (Lucia 2004). In mud-supported facies classes, small euhedral dolomite rhombs are often floating embedded in a matrix of fine-grained micrite increasing porosity only slightly (Fig. 7c).

For mudstone, the porosity was measured in a range of 1.8–4.4% with median of 3.1%. Wackestone samples show a distribution of rather similar range of 2.4–15.0% with median of 5.4%. Compared to results for the corresponding group of limestone, some of the values seem to be unusually high for wackestones (10–15% p.u.) (Fig. 8c). These samples are intensively bioturbated and contain burrows that were completely dolomitized as sucrose dolomite rhombs with abundant intercrystalline pores (Fig. 6).

Besides those bioturbated samples, the distribution for packstone and grainstone indicates distinctly higher values across almost the whole range. Porosity for packstone was measured between 4.1 and 5.8% with a median of 4.9%, compared to 7.6–17.3% for grainstone with a median of 11.7%.

The results for dolostone samples were categorized by size of dolomite crystals into three groups: fine crystalline, medium crystalline, and coarsely crystalline (fine-X, medium-X, coarsely X). The fine- and medium-X samples display a very wide positively skewed distribution of 0.3–18.4% with a median of 2.6% for fine-X and 0.7–13.8% with a median of 3.1% for medium-X dolostone. For coarsely X dolostone, porosity is overall higher with a distribution from 1.9 to 16.3% (median of 8.2%), which shows a rather uniform distribution.

Despite the positive correlation of porosity with increasing particle size observed in limestone and dolomitic limestone, this relation seems to be affected by crystal morphology and secondary porosity of dolostone samples. All three groups are characterized by a distribution with high variance (Appendix 5, Fig. 8d). The highest porosity values were measured for fine-X and coarsely X dolostone consisting of idiomorphic dolomite rhombohedrals which form a framework around abundant intercrystal pores (Fig. 7d).

The effective porosity is distinctly affected by irregular occurrence of vuggy porosity (Fig. 7e). Due to the large volume of the measured sample plugs, they can contain abundant vugs that distinctly influence the result of matrix porosity. Vugs can be both connected and isolated pores and thus participate or not in the effective pore network (Koch 2000; Lucia 2007). However, vugs located inside the rock cylinder cannot be quantified without further investigation methods such as μCT and can therefore not be considered here. An indicator for the presence of numerous isolated vugs could be a relatively low reading of grain density. These pores cannot be penetrated by the medium (gas, water) used for porosity determination, thus adding to the rocks grain volume and reducing the grain density of the sample.

The effective porosity is also controlled by the morphology of dolomite crystals. Depending on the primary facies and type of diagenesis, dolomite crystals of different size and morphology may develop during dolomitization. The morphology of crystals, in turn, is decisive for the type of pore space to be formed. Typically, dolostones composed

of poorly evolved dolomite crystals (nonplanar, xenomorphic) and moderately evolved crystals (subhedral, Planar-s, hypidiomorphic) possess a rather low porosity due to missing intercrystalline pores. Perfectly grown crystals (euhedral, Planar-e, idiomorphic) form some kind of sucrose framework with significantly larger intercrystalline pores and therefore high porosity (Böhm et al. 2010; Lucia 2007; Sibley and Gregg 1987).

On the contrary, the closure of intercrystal porosity by overgrowth of existing crystals due to further dolomitization during deep burial (Fig. 7f) can also reduce rock porosity distinctly ($\phi_{\mathrm{eff}}^{\mathrm{w}} < 5.0\%$) (Lucia 2007).

Significance of porosity data for geothermal projects The widespread porosity distribution of the Upper Jurassic Malm aquifer reflects the heterogeneous architecture of lithology and facies of this sedimentary succession. The aquifer explored in the boreholes MSC-4 and DGF-FB can be divided into three characteristic units based on porosity determination on rock core samples from the buried aquifer. The lowermost part of the aquifer (Malm α–γ) shows the lowest porosity values and practically no dolomitization. It can therefore be interpreted as a rather hydraulically inactive zone and is usually no target for geothermal projects. The aquifer zone actually targeted in the middle part of the Upper Jurassic sequence (Malm δ–ε), is completely dolomitized, but still shows relatively low porosity in the investigated wells. However, irregularly distributed zones with abundance of vuggy porosity and commonly intense karstification can enhance the connection of the borehole to the matrix porosity of the aquifer rock and improve the productivity of the well (Böhm 2012). When dolomitized, the Malm δ–ε therefore represents the most promising target for geothermal exploration in South Germany (e.g., Pullach Th 2 well) (Böhm et al. 2010). Highest, as well as lowest porosities, occur in the upper part of the aquifer (Malm ζ 1–5). Due to the high heterogeneity of the lithofacies, the porosity is strongly dependent on the type of facies and grade of dolomitization in these units. Dolomitized zones with highly developed intercrystal porosity and occurrence of interconnected vuggy porosity, as well as uncemented peloidal grainstones may represent zones of higher hydraulic activity in the upper Malm. However, the uppermost Malm generally consists of micritic and mud-supported limestone beds of a restricted basin facies, which have rather low effective matrix porosity and are therefore more of an aquitard than an aquifer.

Permeability

Whereas porosity is an important parameter that controls the availability of pore space for storage of fluids, the permeability of an aquifer rock mainly depends on the effective porosity and thus the connection between the pores (Koponen et al. 1997). Knowledge of the porosity gives at most an indication of whether the rock matrix could possess a low or high permeability. Geometry and pore size and especially the connection between pores (pore throat size) are also important in order to make valid statements about permeability, especially in the case of very heterogeneous carbonate deposits (Lucia 2007). Information on pore space geometry can be obtained by detailed and complex investigations based on digital image processing of thin sections (PIA) or investigations with mercury injection capillary pressure (MICP) (Anovitz and Cole 2015; Ehrlich et al. 1984). However, both methods can only provide information for a rather small sample

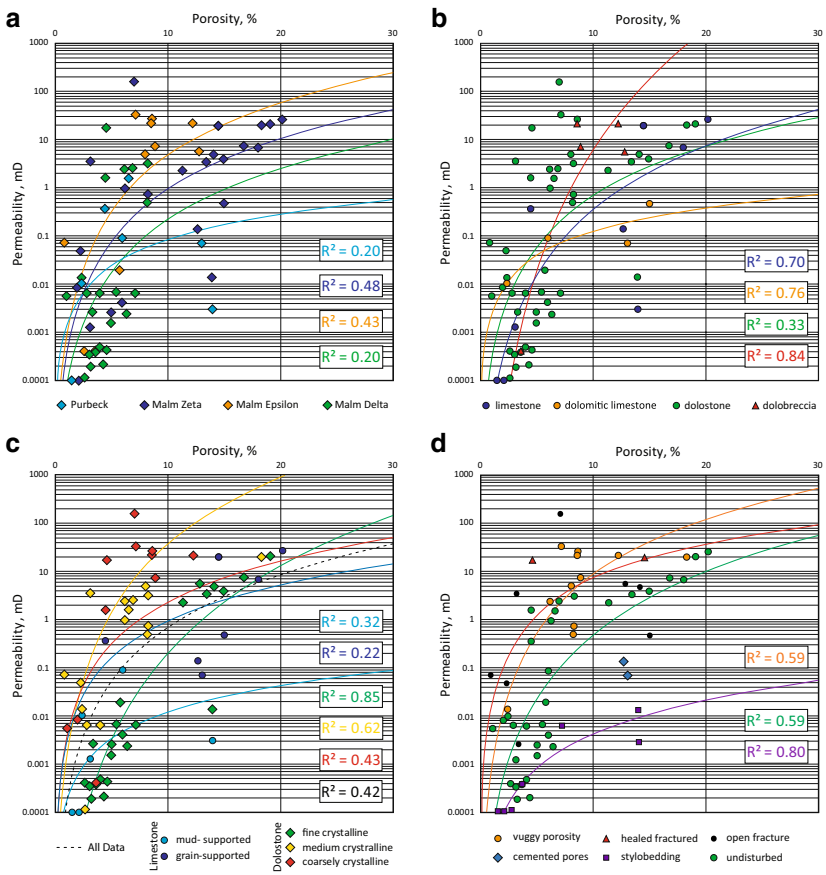

Fig. 9 Porosity–permeability relationship for measured core samples. To improve correlation, the data set was subdivided according to stratigraphic units (**a**), different lithologies (**b**), distinct petrographic rock fabrics (**c**), and secondary characteristics (**d**). Note logarithmic scale for permeability—colored lines represent power lines for each class

volume and destroy the sample. Moreover, PIA can only provide information on a two-dimensional relationship of the pore network. In order to establish a general porosity–permeability relationship without having information on pore geometries, e.g., for drilling projects with suitable borehole logs but without rock cores or cutting samples due to high circulation losses, a statistical approach should be used that allows permeability estimation based on porosity and information on rock fabric. To determine these empirical correlations, the results of the permeability measurements on 63 core samples were correlated with the respective results of the porosity studies.

Porosity–permeability relationship of laboratory measurements

The correlation was tested in the context of various aspects to find a reliable relation between porosity data and permeability. Figure 9 shows the poro–perm relation found for the Malm aquifer at locations MSC-4 and DGF-FB regarding stratigraphic units, lithology, facies, and secondary features like fractures, dissolution (vugs) or the presence of stylolites. Poro–perm based on stratigraphic units shows a barely satisfying relationship of hydraulic properties (Fig. 9a). However, similar to porosity distribution,

permeability tends to be higher in the Malm ζ units than in Malm δ with exception of some samples from Malm ε which reflect high permeable zones due to brecciation. The relationship between porosity and permeability as a function of lithology shows a slightly better correlation (Fig. 9b). Dolostones tend to have a higher permeability than limestone or dolomitic limestone, which are only well permeable at relatively high effective porosity (> 12%). However, the correlation is still not satisfying for transferability of results as it may be dependent on a more distinct petro-fabric within each lithological group. Figure 9c shows the porosity–permeability relationship for different limestone classes (including dolomitic limestone) and dolostone fabrics. The correlation for dolostone indicates higher permeability with increasing size of dolomite crystals. Fine-X dolostone was mostly found to be poorly permeable for rather low porous samples, whereas medium-X and coarsely X dolostones tend to higher porosity and permeability. However, the correlation within these groups still shows some scattering as crystal morphology has significant impact on the permeability of dolostones (Böhm 2012; Sibley and Gregg 1987).

Poro–Perm relationship for different limestone facies was difficult to address and might be affected by bias due to a rather low availability of permeability data. Even after a long test duration (several days), it was not possible to generate a stationary flow for some of the mud-supported limestone samples (mudstone, wackestone, packstone), which can therefore be interpreted as technically impermeable ($k < 10^{-5}$ mD). The permeability for mud-supported limestones is generally microporous with only rare interparticle or intercrystal pores and exhibit permeabilities lower than 0.1 mD. On the contrary, grain-supported limestones (packstone, grainstone, floatstone) exhibit moderate-to-good permeability if interparticle pores are not affected by cementation. Some samples show a rather low permeability compared to their porosity—these samples were affected by partial cementation of interparticle pores or formation of stylolites reducing permeability significantly (compare Fig. 7b).

General limitations in interpreting permeability data of the Malm reservoir

The Malm reservoir in the Bavarian Molasse Basin is generally defined as fracture- and karst-dominated porous aquifer (Fritzer 2012, Konrad et al. 2019). The hydraulic properties of the reservoir can therefore to a certain extent be interpreted as dual porosity and preferential flow. Alternation of facies depending on the depositional environment of the Malm as well as karstified or vuggy zones along bedding planes can result in an anisotropic hydraulic behavior of the strata. Unfortunately, most of the permeability data could only be measured perpendicular to bedding during this research due to technical reasons of sample dimensioning.

As both investigated wells are near vertical and bedding of the strata is more or less horizontal, the anisotropy could have a significant influence on the characterization of the flow zones. The impact of directional permeability was therefore examined exemplarily for different fabrics and facies types using the air-driven permeameter (Fig. 10). For non-vuggy carbonate samples the results show 2–30% higher horizontal permeability, but it can increase to about + 200% when abundant vugs are accumulated parallel to the bedding and connected to the pore network. On the contrary, the occurrence of vugs

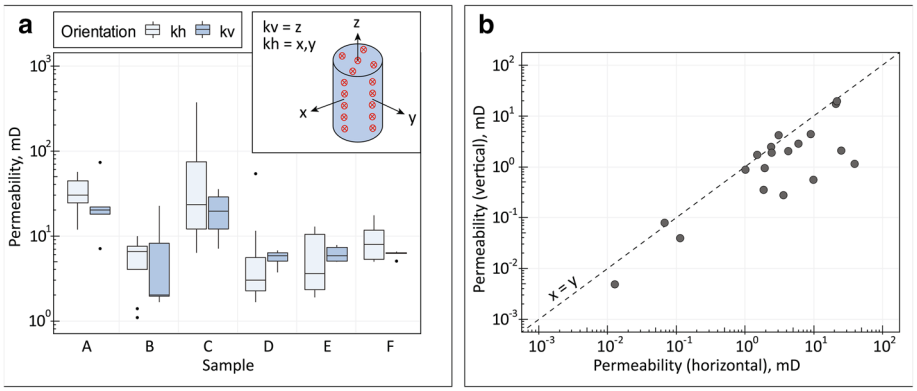

Fig. 10 Verification of directional permeability caused by anisotropy of rock samples. **a** The measurements are distributed along each spatial dimension of the cylindrical plug to generate vertical (*k*v) and horizontal (*k*h) permeability information. Horizontal permeability generally shows a higher variance due to vertical variations in deposition. Sample C contains abundant vugs along the cylinder, which significantly increase the horizontal permeability, while the vertical permeability of sample F is reduced due to stylobedding. **b** Permeability anisotropy for all samples measured with the air-driven permeameter, which often show a higher permeability in the horizontal direction

does not appear to effusively increase the permeability perpendicular to the bedding of the studied samples. The vugs mostly represent a separate-vug pore space, whereas their contribution to the effective pore network depends on the prevailing interparticle/intercrystal porosity. Furthermore, samples with lamination and stylobedding showed a reduced permeability perpendicular to bedding by about an order of magnitude (Fig. 9d).

A further limitation in the interpretation of the generated data set is the irregular occurrence of fracturing or karstification throughout the Malm aquifer. While the impact of karstification cannot be covered in this paper, some of the "highly" permeable samples are associated with open fractures or fissures that increase the permeability (Fig. 9d). However, fractures were also observed for some low permeable samples indicating that fracture orientation could be a controlling factor and directional permeability can vary accordingly.

Empirical permeability estimation model

Based on the discussed porosity–permeability relationship measured on rock cores, an empirical permeability estimation model was developed that should be valid for the Malm aquifer and can be used for regional transfer. The poro–perm relationship for the complete data set of this study was found by the power law (21):

$$k_{\text{all}} = 0.0003 * \phi^{3.37} \quad \text{with} \quad R^2 = 0.36, \tag{21}$$

where k_{all} is the permeability in millidarcy (mD) and ϕ the core porosity effective for water (in %).

However, the typical permeability variations of a heterogeneous carbonate aquifer are averaged if the entire data set is correlated at once (Lucia 2007). The low coefficient of determination reflects this problem since detailed information about the rock fabric, the

associated pore geometry, and the influence of the secondary porosity were not taken into account. By subdividing data into respective petrographic rock classes (lithology, particle/crystal size) more reliable relationships were established:

$$k_{\mathrm{Lms}} = 2.0\mathrm{E}^{-04} * \phi^{3.10} \quad \text{with } R^2 = 0.49, \tag{22}$$

$$k_{\mathrm{Lgs}} = 7.7\mathrm{E}^{-03} * \phi^{2.64} \quad \text{with } R^2 = 0.88, \tag{23}$$

$$k_{\mathrm{fX}} = 9.0\mathrm{E}^{-08} * \phi^{6.47} \quad \text{with } R^2 = 0.94, \tag{24}$$

$$k_{\mathrm{mX}} = 2.0\mathrm{E}^{-04} * \phi^{4.40} \quad \text{with } R^2 = 0.78, \tag{25}$$

$$k_{\mathrm{cX}} = 3.9\mathrm{E}^{-03} * \phi^{3.97} \quad \text{with } R^2 = 0.86, \tag{26}$$

$$k_{\mathrm{Sb}} = 2.0\mathrm{E}^{-05} * \phi^{2.33} \quad \text{with } R^2 = 0.80, \tag{27}$$

where Lms = mud-supported limestone, Lgs = grain-supported limestone, fX = fine crystalline dolostone, mX = medium crystalline dolostone, cX = coarsely crystalline dolostone, and Sb = stylobedding.

In order to create a valid relationship that depends only on these petrographic rock classes, samples showing secondary characteristics which biased the measured permeability were excluded. Samples that contain open fissures are expected to have a significantly increased permeability and have therefore been excluded. Two limestone samples showing sparitic cementation of the pore spaces in the thin sections have also been excluded. Cementation can occur to varying degrees and significantly affect porosity and permeability. The models can therefore not reliably estimate the permeability for these sample types. Depending on the degree of fracture and cementation, permeability fluctuations of up to two orders of magnitude are to be expected and must be taken into account accordingly for these secondary characteristics.

Limestone and dolomitic limestone samples were separated into mud-supported and grain-supported fabric classes as well as samples showing stylobedding (Fig. 11a). The empirical power law for each of these classes shows an overall better fit compared to that based on the whole data set. Permeability of mud-supported limestones is significantly lower than for grain-supported limestones due to microporosity, smaller pore throats, and absence of interparticle porosity (Figs. 9c, 11a). The lowest permeability values can be expected for samples affected by stylobedding when stylolites are orientated perpendicular to flow direction (Fig. 11a). However, the reduction in permeability caused by stylolites still seems to have a relation to the effective porosity for this data set, but might be valid only when stylobedding is oriented perpendicular to flow direction.

In order to find a valid relationship for dolostone, the data set was separated into classes according to the prevailing dolomite crystal size. Coarsely X dolostone shows the highest permeabilities, followed by medium-X dolostone with fine-X dolostone tending

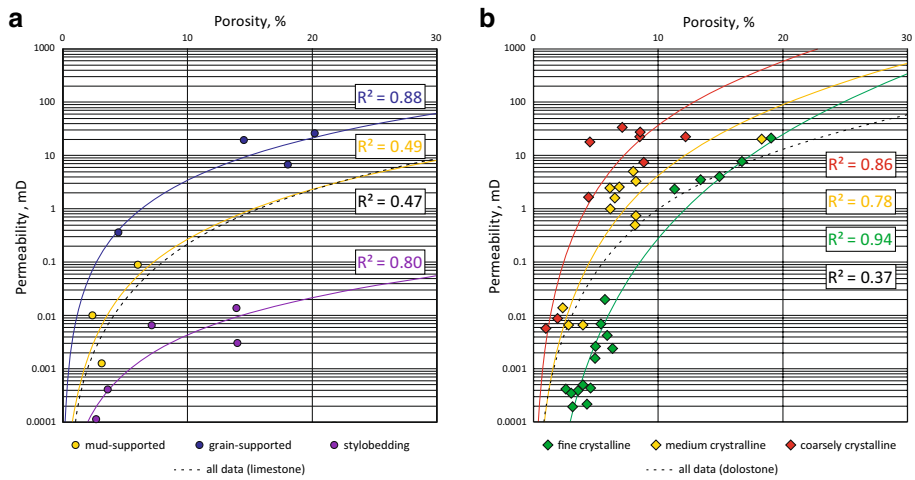

Fig. 11 Empirical poro–perm relationship for distinct petrographic classes excluding samples showing secondary porosity (fractures, vugs). Limestones and dolomitic limestones (**a**) show significant difference in the poro–perm relationship compared to dolostones (**b**). Dolostones tend to higher permeability with increasing porosity than limestone and dolomitic limestone classes. The lines represent power laws for each individual class

to rather lower permeabilities (Fig. 11). However, the hydraulic properties of dolostone are not only controlled by crystal size, but also by the morphology of crystals. Dolostone composed of idiomorphic dolomite rhombs mostly shows a network of porous and permeable intercrystal pores.

Overall, the assignment of the rock samples to different petrographic classes indicates a significant improvement in the porosity–permeability relationship for this data set.

Validation and discussion of permeability models

In addition to the empirical model based on laboratory data of this study, pre-existing models were adopted and tested. Permeability was calculated by the GPPT (18), the model of Berg (19) as well as the RGPZ model (20) using different cementation factor estimations (9)–(13). Comparing the measured permeability to that calculated by the different models, best fit was found for the model of Berg at the well MSC-4 and the empirical model of this study for the well DGF-FB (Fig. 12). Most models show an underestimation of permeability up to two orders of magnitude for the well M-SC4, especially in vuggy and fractured zones in the lower well section (Fig. 12a). The measurement of porosity of vugular carbonate samples using the WIP method is usually corrupted due to the loss of saturation and results in an underestimation (Appendix 2). However, these vugs do not necessarily participate in the flow through the rock matrix, but estimation of permeability as a function of porosity will be biased. The fracture zones, in turn, can have significantly higher permeabilities if the fractures are open and offers preferred flow paths. In order to avoid a general overestimation of the permeability of fracture zones, a conservative approach was chosen, whereby core samples with open fractures/cracks were not considered in the empirical models.

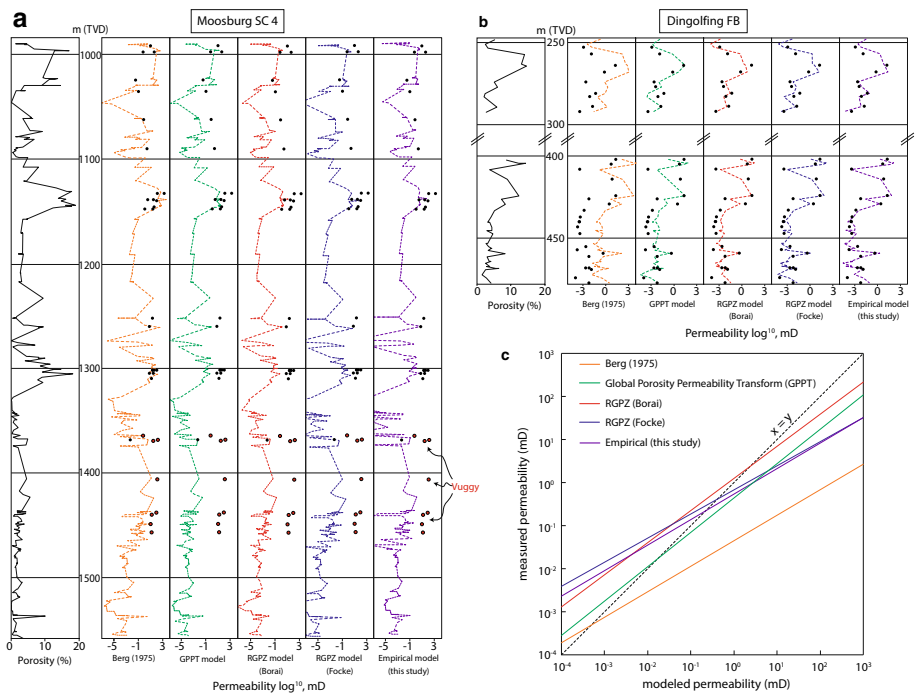

Fig. 12 Comparison of different permeability models with the permeability of rock cores. **a** Most models seem to underestimate the permeability compared to core permeability of the Moosburg SC4 well, especially in vuggy zones in the lower well section. **b** Besides the Berg model, all models show a relatively good fit for the well Dingolfing FB to permeability measured on rock cores. **c** Correlation of the measured and modeled permeability in a log–log plot to validate the model quality. The GPPT model seems to be the most reliable model based on the data set

The models can therefore not include secondary porosities, such as karst, associated vugs or open fractures satisfactorily in the calculation. However, all models can reflect the prevailing permeability trend quite well. For the well DGF-FB, all models except the Berg model show a fairly good fit to the core-derived permeability (Fig. 12b). The permeability modeled by the Berg model shows a significant overestimation compared to core data of up to three orders of magnitude. The mean particle/crystal size appears to have a greater influence on this model than on the other models. At the well DGF-FB, dolostones with medium-to-large crystals are very common, but the further growth of crystals reduces the pore space and therefore the permeability is rather low. This case can apparently not be reproduced sufficiently by the Berg model. On the contrary, the empirical model developed in this study shows the highest accuracy. For almost all samples of the well DGF-FB, the permeability was measured in addition to porosity, which allows a more robust empirical relationship than for the well MSC-4. For estimation of permeability with the empirical model, however, a detailed description of the type of rock and particle/crystal size is required.

For model validation, measured and modeled results were correlated in a log–log plot (Fig. 12c). All models show an underestimation for measurements of low permeability and an overestimation for measurements with high permeability. The Berg model overestimates the permeability for almost all measured rock cores up to several

orders of magnitude (except for the vuggy zones of the MSC-4). On the contrary, the RGPZ models and the empirical model show a much better fit, but still deviate by about an order of magnitude for min/max permeabilities. Overall, the GPPT model shows rather small deviations from the core measurements (less than one order of magnitude). Larger deviations occur only in the high permeability range. The GPPT model seems to have even a higher accuracy than the empirical model at MSC-4. If no detailed information on the lithofacies is available, the GPPT model can therefore be used for permeability estimation. Since the model is based on a classification of the reservoir rock into distinct rock fabric numbers (rfn), which can also be determined by the interpretation of image logs, no precise information on particle/crystal size is required.

Distribution of resulting permeability throughout the Malm reservoir

The results of the investigated wells show a very broad distribution of permeability scattered over several orders of magnitude from less than 10^{-6} mD to a maximum of 10^{2} mD. This high variation reflects the heterogeneous character of alternating lithologies and facies within the sedimentary Malm reservoir. Figure 13a shows the permeability distribution for the different Malm units and the overlying Purbeck for the core-derived and modeled data set. A detailed overview of permeability distribution for each stratigraphic unit can be found in Appendix 6.

The lower sections, Malm α–γ show the lowest permeabilities with only minor variations for the well MSC-4. The permeabilities for this section of tight bedded limestones range from $2 * 10^{-6}$ mD to a maximum of $7.9 * 10^{-1}$ mD reflecting rather poor suitability

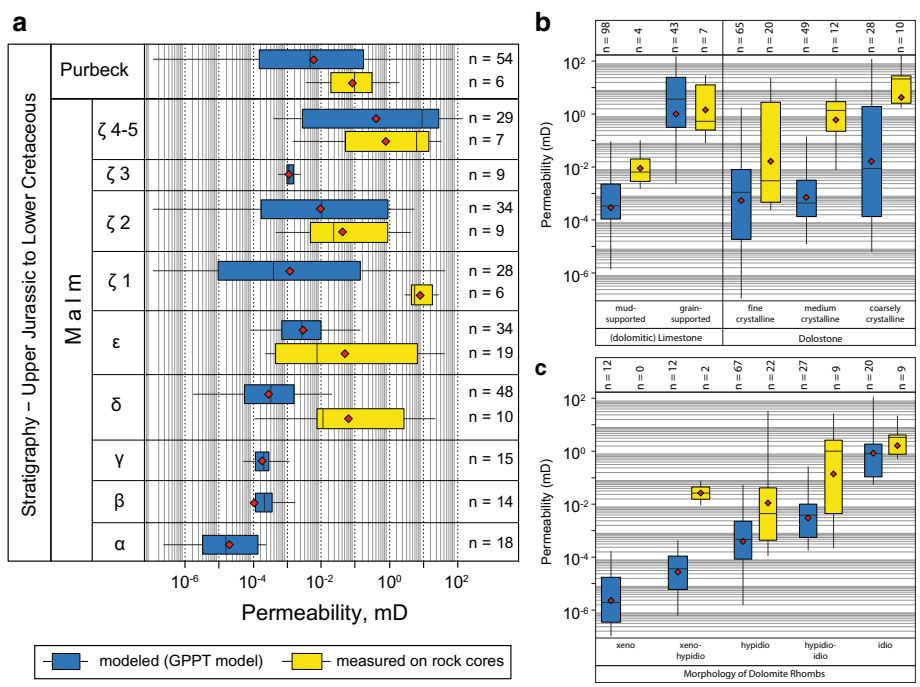

Fig. 13 Distribution of permeability measured on rock cores compared to permeability modeled by the GPPT. **a** Distribution within the stratigraphic units of the Malm reservoir. **b** Dependence of permeability on particle and crystal size as well as on the morphology of dolomite crystals (**c**)

as a reservoir. The middle part of the reservoir (Malm δ–ε) shows up to five orders of magnitude higher permeabilities, but also a higher variance than the lower units. Permeability data derived by the GPPT model range from at least 6 * 10^{-6} mD to 12 mD for these units. However, the permeability measured on rock cores show significantly higher values (up to 144 mD) than those estimated by the GPPT model. This section consists almost entirely of dolostone with varying size and morphology of dolomite crystals. Additionally, locally abundant occurrence of vugs and intense fracturing may enhance the permeability of the rock. These conditions cannot be included in the models and therefore lead to an underestimation of permeability.

The uppermost units, Malm ζ 1–5 together with the overlying Purbeck show a permeability variation over several orders of magnitude which reflects this highly heterogeneous part of the reservoir. The permeability ranges from as low as 10^{-6} mD for mud-supported bedded limestone and very fine crystalline and compacted dolostone up to 120 mD for a ooidal–peloidal grainstone with high interparticle porosity. Due to the heterogeneous depositional character of these units (see Fig. 1), permeability can be expected to vary widely in a vertical as well as lateral direction throughout the reservoir.

By comparing permeability with regard to lithology, no significant differences between limestone and dolostone can be found for the population of the investigated data set (Fig. 14a). Both lithologies show a normal permeability distribution with a high variability. On average, both groups show permeabilities in the order of 10^{-3} mD, with dolostones achieving a slightly higher permeability. Dolomitized limestones have an average permeability of about one order of magnitude higher than limestone and dolostone (10^{-2} mD).

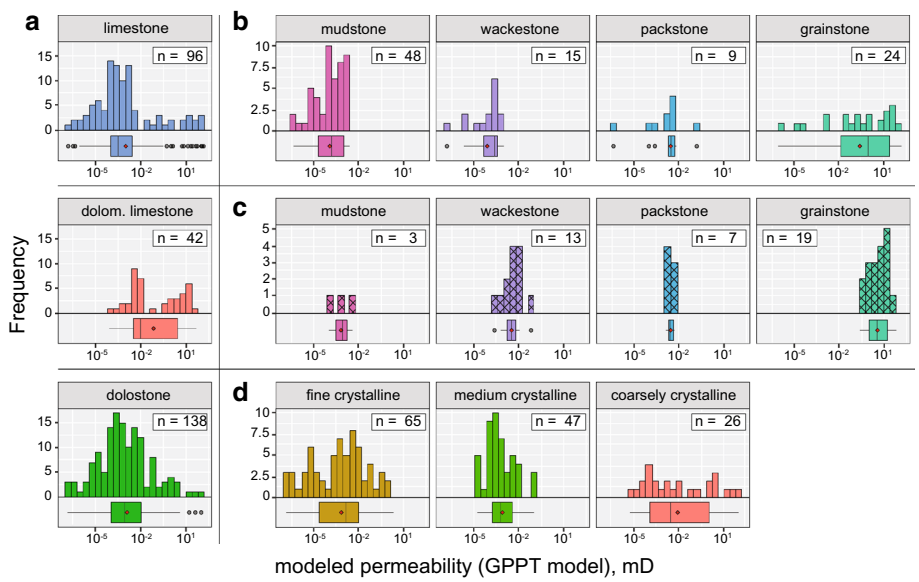

Fig. 14 Distribution of the permeability modeled by the GPPT for different lithology and facies classes. **a** The permeability is normally distributed within the limestone and dolostone groups, but shows a wide scattering over several orders of magnitude. Dolomitic limestone shows on average higher permeability with a bimodal distribution. **b**–**d** The permeability tends to be higher with increasing particle size for (dolomitic) limestone. Dolostone shows a similar correlation with the crystal size, but not as pronounced as for the limestone groups

The comparison of the permeability for different lithologies and rock fabrics shows a dependence on the particle and crystal size, i.e., the interparticle and intercrystal porosity, available for the flow through the rock matrix (Fig. 13b). Whereas mud-supported (dolomitic) limestone facies exhibit a rather low permeability, grain-supported facies types can reach permeabilities of up to 100 mD. Grainstones composed of ooids and peloids usually show distinctly higher permeability than mud-, wacke- or packstones if the pore space is not cemented by sparry calcite—especially when dolomitized (Fig. 14b, c). A similar trend towards increasing permeability with increasing crystal size was observed for the dolostone samples (Figs. 13c, 14d). However, the relationship is not as clear as for limestone facies, since permeability is controlled not only by the crystal size, but also by the morphology of the dolomite crystals (Fig. 13c). Ideally, grown dolomite crystals with clear crystal boundaries exhibit a large number of intercrystal pores in a crystal-supported pore network that usually exhibits high permeabilities (see Fig. 7d). The permeability for dolostones composed of large idiomorphic dolomite crystals was measured within a range of 1–120 mD reflecting good-to-very good reservoir quality. Dolostones composed of xenomorphic dolomite crystals without clear crystal boundaries exhibit very low permeabilities, independent of the dominant crystal size (see Fig. 7f). The permeability of these types of dolostones can be as low as $1 * 10^{-6}$ mD since no pore network is available for the flow of fluids. A detailed overview of permeability distribution for the different lithologies, rock fabrics, crystal sizes, and crystal morphologies is also given in Appendices 7 and 8.

Scale of observation and transfer of parameters for regional interpretation

The interpretation of hydraulic properties of a reservoir is usually tied to the problem of different observation scales and detailed information about the aquifer rock. The investigation of rock properties on a pore scale (microscale, e.g., microscopy, tomography) may differ from the properties measured on the core scale (macroscale, e.g., HEP, WIP, triaxial flow test) due to the heterogeneity of the rock matrix, particle size, and pore size on different scales. By transferring these parameters to a regional reservoir scale or even to a basin scale, further properties such as fractures, faults(-systems), karstification, diagenesis, and a spatially heterogeneous lithostratigraphic distribution will influence the hydraulic behavior of the reservoir. Therefore, different factors on different scales control the hydraulic and geothermal field of a basin reservoir. These factors are strongly dependent on the distribution of petrophysical rock properties, which should be investigated on both laboratory and field scale (Kumari and Ranjith 2019; Scheck-Wenderoth et al. 2014).

The matrix properties measured in this research on a core scale refer to the aquifer matrix, which summarizes all heterogeneities below the reservoir scale, such as changes in facies, particle sizes, vugs, stylobedding, and fissuring of the rock samples. The measured rock cores thus represent a continuous volume of averaged properties of the pore scale and are defined here as representative elementary volume (REV) within a centimeter range for interpretation of hydraulic rock properties (Bear 2013; Hommel et al. 2018; Konrad et al. 2019). The porosity and permeability data set can therefore be used for the parametrization of models at different scales by using the different distributions for the facies (core and reservoir scale, Appendices 5, 8), the lithology (reservoir scale, Appendices 4, 7) or the stratigraphy (basin scale, Appendices 3, 8) depending on the scale and

detail of the model. However, the REV investigated in this study cannot be considered representative on the reservoir and basin scale alone, without considering the superordinate properties (e.g., karstification, faults, diagenesis). Therefore, porosity and permeability could be underestimated if the data set measured at the rock cores has to be upscaled for regional transfer without further information from geophysical well logs.

In order to validate a regional transfer of hydraulic properties from the investigated wells MSC-4 and DGF-FB to the area of Munich, the porosity data measured on the rock cores were compared to the porosity calculated from an electrical downhole log of the Munich well (Fig. 15). Porosity is plotted as a function of natural gamma radiation (gamma ray), the only available log for the well MSC-4, to implicate the petrographic character for both locations. In addition, the data were grouped by their respective stratigraphic units to show the distribution of porosity for each of these units. The correlation of the data generally shows a good agreement of porosity distribution for each stratigraphic interval. However, the effective porosity measured on the drill core samples appears to be slightly lower as the Archie porosity calculated from the log refers to the total porosity (including isolated pore space). It can therefore be assumed that the effective porosity for the borehole near Munich is somewhat lower than the calculated Archie

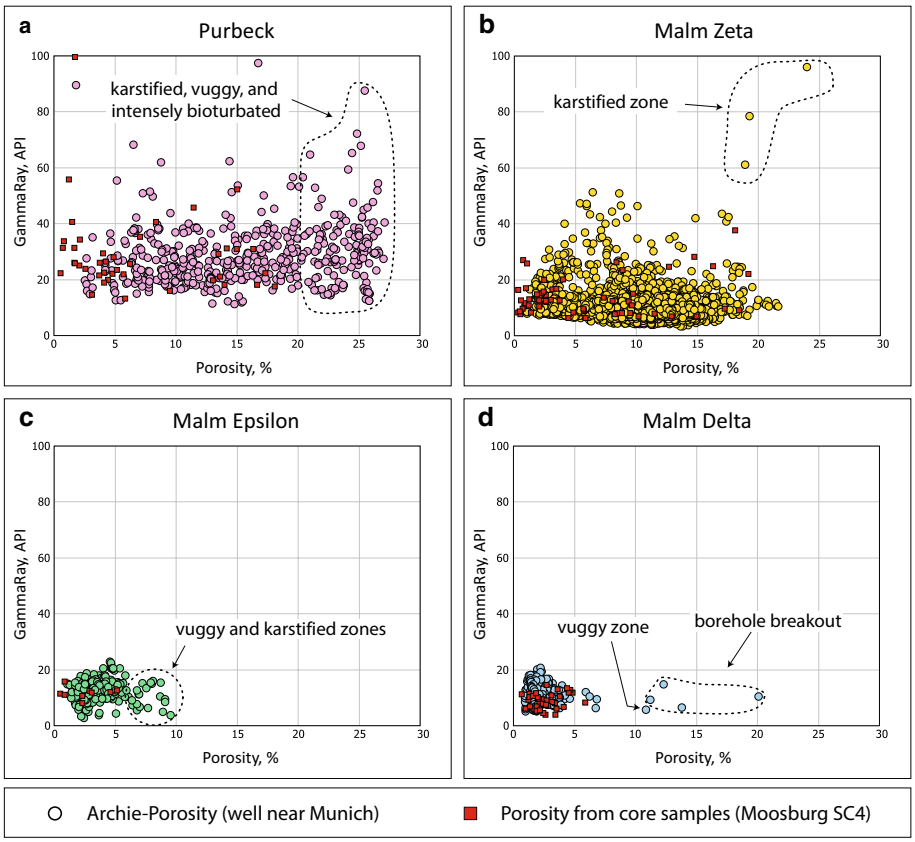

Fig. 15 Correlation of the porosity data from rock cores (Moosburg SC4) to calculated Archie porosity from the downhole deep resistivity log of a geothermal well in the area of Munich. By subdivision of data into the stratigraphic intervals Purbeck (**a**), Malm Zeta (**b**), Malm Epsilon (**c**) and Malm Delta (**d**), almost similar distributions of porosity can be found for both boreholes. Note that Archie porosity represents total porosity of the reservoir rock including isolated pores and secondary porosity (vugs, karstification)

porosity. Similar to the MSC-4 and DGF-FB data sets, the porosities interpreted from the well log are widely scattered both in the upper Malm units and in the Purbeck. Log porosity shows a range of 2.5–27.0% for the Purbeck and 1.0–24.0% for the Malm ζ. Porosities exceeding 20% were calculated for zones where karstification, vuggy layers or intense bioturbation were identified by the interpretation from Image Log and could not be covered by rock core analysis (Fig. 15a, b). The widely scattered gamma ray measurements also reflect very heterogeneous deposition for those units (5–100 API units). The middle and lower parts of the reservoir (Malm δ–ε), on the other hand, appear to be much more uniform and show a porosity range between 0.5 and 6.5%. Porosities higher than 6% correlate with locally occurring vuggy and karstified zones in unit Malm δ at the well near Munich, which were detected during the interpretation of the image log (Fig. 15c). At Malm δ, porosity values higher than 11.5% were caused by an intense borehole breakout, which is probably an indicator of a vuggy/karstified zone and eventually resulted in erroneously low resistivity readings of the electrical log at this depth (Fig. 15d).

Figure 16 shows a trans-sectional correlation of hydraulic parameters from the wells northeast of Munich to the geothermal well in the Munich area. The distance between each well is about 40 km. For the wells MSC-4 and DGF-FB, the porosity and permeability data were measured on rock cores. In addition, a permeability log using the GPPT model was estimated to cover rock samples without permeability measurement. The data set for the well near Munich, however, is based exclusively on the interpretation of geophysical downhole logs. The porosity was calculated from the electrical resistivity log while petrographic rock types were derived by interpretation of gamma ray and Image

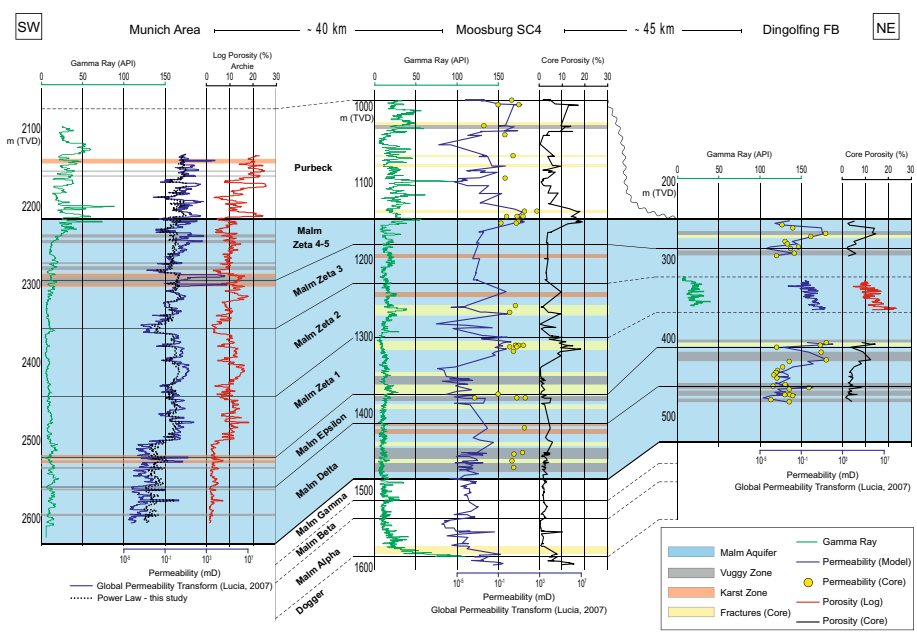

Fig. 16 Correlation of hydraulic parameters for the Malm aquifer in a SW–NE section from Munich to Dingolfing. Porosity and permeability were measured on rock cores for the wells MSC-4 and DGF-FB—permeability logs were calculated by permeability models (blue lines). Gamma ray was measured and porosity log calculated by electrical resistivity logs. Karstified and fractured zones were identified by Image Log (Munich well) or by rock core description. Note logarithmic scale for permeability

Log and subsequently were translated to rock fabric numbers (rfn) according to Lucia (2007). The permeability log was then estimated by the GPPT model. Secondary porosity (vugs, fractures) and karstified zones were identified by the Caliber Log and Image Log (Munich well) or the description of rock cores when vugs, or cavities enlarged by karstification could be observed (MSC-4, DGF-FB).

As the Malm aquifer in the Munich area is buried significantly deeper (TVD 2215 m) than in the investigated wells DGF-FB (TVD 243 m) and MSC-4 (TVD 1115 m), it must be assumed that the in situ pressure and temperature conditions have a negative influence on the porosity and permeability at this depth. Hedtmann and Alber (2017) and Homuth et al. (2015) reported a reduction of permeability in the order of magnitudes considering the effective pressure and temperature conditions in this depth. To allow an accurate comparison between log data and core data, various conversions must be found for each lithofacies type and for different stress and temperature conditions. However, this research focuses on general porosity and permeability trends in the context of the heterogeneous Malm aquifer, and the effects of in situ conditions have therefore been neglected for the time being.

In general, the models show a rather similar pattern for the hydraulic matrix properties within the reservoir at the investigated wells. The Purbeck and Malm ζ 4–5 units show a high variance of poor-to-reasonably well-permeable layers in the well near Munich, reflecting the heterogeneity of sedimentary deposits of the uppermost Malm. These units are represented with reduced thickness in the wells MSC-4 and DGF-FB (Purbeck is missing at DGF-FB), but show a rather similar appearance in lithology and facies. Possible permeable flow zones are expected in karstified, fractured, and vuggy horizons as well as layers of grainstones composed of peloids, ooids, and fossil fragments which contain abundant interparticle pores. These grainstone layers were found in both wells MSC-4 and DGF-FB showing effective porosities up to 18% and permeabilities of 10^1 mD and can be expected to be also present at the Munich well. Throughout the units Malm ζ 1 – 3, fluctuation of hydraulic properties is common at all wells. Permeable zones of often fractured and vuggy, dolomitized limestone and dolostone were observed on rock cores of units of Malm ζ 1–2 (MSC-4 and DGF-FB). For the well near Munich, no reliable indications were found for such vuggy zones, but intense karstification was interpreted from Image Log and Caliber Log at the transition to Malm ζ 2. Brecciated dolomitic limestones and dolostones were found at the basal layers of Malm ζ 1 at MSC-4 and DGF-FB, indicating a layer of rubble and debris of a nearby reef. Depending on the grade of dolomitization, this layer can be rather well permeable. At the DGF-FB well, this layer is well dolomitized and a rather high permeability of 10^2 mD was measured on core samples. In the well near Munich, these layers are interpreted from Image Log to be represented by a massively bedded layer composed of fossil debris and lithoclasts. However, dolomitization seems to be not as advanced as at the well DGF-FB here. The low porosity interpreted from resistivity log (< 5%) therefore suggests a rather low permeability (10^{-2}–10^{-3} mD) as this layer might be mud-supported here. The lowermost units of the reservoir (Malm δ–ε) are mainly composed of dolostone at the wells MSC-4 and DGF-FB and show rather low porosities (< 5%) and permeabilities (< 10^{-1} mD) compared to the overlying units. However, in locally occurring vuggy, fractured, or karstified horizons higher permeabilities could be observed. For the well near Munich these units

are interpreted to be composed of massive bedded limestones showing some degree of dolomitization and locally occurring vuggy layers. A fractured and karstified horizon was interpreted at the top of Malm ε indicating a possible flow zone.

Conclusion

The results of laboratory measurements on 363 rock core samples of the wells Dingolfing FB and Moosburg SC4 show that the hydraulic properties of the rock matrix within the Malm reservoir are strongly dependent on lithology and facies. Due to the heterogeneous nature of the Upper Jurassic deposits, focussing on rock characteristics such as lithology and facies allows a more distinct estimation of porosity and permeability. By subdividing the data into corresponding groups, the widespread ranges of effective porosity and permeability could be limited based on basic attributes. As a result, a comprehensive data set of the effective porosity and permeability controlled by the rock matrix of the Malm aquifer was developed, which is subjected to variation of stratigraphy, lithology, and facies. The data set can consequently be used for the estimation of hydraulic properties of the rock matrix based on information of past and present geothermal projects to extend the knowledge about spatial distribution of rock parameters within the reservoir. The porosity data set and permeability estimated from the empirical porosity–permeability relationships form a good basis as input parameters for hydraulic and geomechanical models.

The interpretation of the results from laboratory measurements indicate that good hydraulic properties of the rock matrix are mainly restricted to grain-supported rock fabrics and strongly dolomitized layers throughout the reservoir. Especially when vuggy, fractured or karstified zones are combined with a rock matrix of good hydraulic properties, very productive flow zones can be expected in that part of the reservoir. However, a quantitative prediction of the hydraulic productivity on a reservoir scale resulting from fracturing and/or karstification cannot be covered within the limits of this parameter study.

The investigated wells showed that the upper part of the reservoir (Malm ζ 3 to Purbeck) is very heterogeneous and often dominated by mud-supported limestone deposits that possess rather poor hydraulic properties. However, locally occurring layers of peloidal grainstones, dolomitized and vuggy or karstified horizons are expected to possess good hydraulic properties and are possible flow zones in the upper part of the Malm. The middle section of the reservoir (Malm δ–ζ 2) showed less heterogeneity, but was almost completely dolomitized in the wells Dingolfing FB and Moosburg SC4. The hydraulic properties of the rock matrix in this section are mainly controlled by the size and morphology of the dolomite crystals. Large, idiomorphic dolomite crystals can form a highly porous and very permeable rock matrix. On the other hand, dolostone, composed of fine crystalline and rather xenomorphic dolomite crystals, as well as pore space reduced by diagenetic compaction lack permeability. However, locally fractured and vuggy areas may strongly favor flow also in this section of the reservoir.

An approach of a possible regional transferability of the collected data set from the wells Moosburg SC4 and Dingolfing FB towards the area of Munich showed a generally similar subdivision of hydraulic properties in the reservoir. The upper and middle part of the reservoir can possess a good productivity if fractures and karstification synergize with good hydraulic properties of the rock matrix in distinct zones. However, the usually

well-dolomitized Malm δ and Malm ε units showed relatively poor hydraulic matrix properties and are more dependent on enhancement by fracturing or karstification.

In order to draw a conclusion for the possibility of regional transfer throughout the Molasse Basin, a precise correlation between different wells is difficult when lacking important downhole logs—but can be done based on estimation and assignment of parameter ranges within stratigraphic units. However, in order to further improve the understanding of the regional contexts within the reservoir, an ongoing process is required that involves further data from wells and projects.

Abbreviations

mD: Millidarcy; THM: Thermal–hydraulic–mechanical; HEP: Helium gas expansion porosimetry; WIP: Water immersion porosimetry; PIA: Petrographic image analysis; MSC-4: Moosburg SC4; DGF-FB: Dingolfing FB; mTVD: Meters total vertical depth; ϕ_{eff}: Effective porosity; $\Delta\phi_{eff}$: Absolute difference of effective porosity; p.u.: Porosity unit; V_b: Bulk volume; V_g: Grain volume; L: Length; u: Diameter; W_d: Dry sample weight; ρ_b: Bulk density; V_t^{He}: Helium grain volume by HEP; V_P^{He}: Pore volume by HEP; ρ_g: Grain density; ϕ_{eff}^{He}: Effective porosity by HEP; W_s^w: Water-saturated sample weight; ρ_w: Density of water; V_P^w: Pore volume by WIP; ϕ_{eff}^w: Effective porosity by WIP; R_0: Electrical resistivity of rock matrix; R_w: Electrical resistivity of formation water; m: Cementation factor; ϕ: Porosity fraction of rock matrix; IP: Interactive petrophysics; k: Permeability; P_p: Confining pressure; MPa: Megapascal; Q_{up}: Upstream flow rate; Q_{down}: Downstream flow rate; Q_{av}: Averaged flow between up- and downstream; μ: Fluid viscosity; ΔP_p: Pore pressure drop; A: Cross-sectional area; T: Device-specific value (Tiny Perm II); k_g: Gas permeability; V: Volume; p: Pressure; Δp: Pressure difference; GPPT: Global porosity–permeability transform; rfn: Rock fabric number; A: Absolute term; B: Absolute term; C: Absolute term; D: Absolute term; Φ_{ip}: Fractional interparticle porosity; mp: Mean particle size; d: Geometric mean grain size; a: Packing parameter; STD: Stratigraphic commission of Germany; n: Count; CJ: *Clypeina jurassica*; CS: *Campbelliella striata*; BR: Bryozoan; X: Crystalline; MICP: Mercury injection capillary pressure; kv: Vertical permeability; kh: Horizontal permeability; R^2: Coefficient of determination; Lms: Mud-supported limestone; Lgs: Grain-supported limestone; fX: Fine crystalline dolostone; mX: Medium crystalline dolostone; cX: Coarsely crystalline dolostone; Sb: Stylobedding; REV: Representative elementary volume; Min: Minimum; Max: Maximum; Med: Median; MAD: Median absolute deviation.

Acknowledgements

We wish to thank the BMW Group as well as Erdwerk GmbH for collaboration and their support in the project High-Temperature Aquifer Thermal Energy Storage (HT-ATES) Dingolfing. Also we thank the Bayerisches Landesamt für Umwelt (LfU Bayern) for the access to stored drilling cores and the cooperative work especially for support of sample preparation, the Chair of Sedimentology (University of Erlangen-Nürnberg) for the possibility to use the TinyPerm II for permeability measurements in their laboratory, Florian Kröner for the help in collecting core samples at the core shed, and all the technicians, colleagues, and students who helped us in handling the instruments and contributed in measurement of data in the laboratories. Finally, we want to thank the three anonymous reviewers for their meticulous revisions, which helped to improve the manuscript considerably.

Authors' contributions

All authors designed the workflow of this study and took part in interpretation of results. DB carried out the individual steps of the presented workflow and was responsible for realization of laboratory measurements and data interpretation. MP was a major contributor in acquisition of rock cores, sample preparation, and interpretation of results. DP was responsible for acquisition and interpretation of downhole logs and PW contributed by interpretation of lithology, facies, and stratigraphy of the reservoir. All authors read and approved the final manuscript.

Funding

This work has been performed in the framework of the project Geothermal-Alliance Bavaria (GAB) and is funded by the Bavarian Ministry of Science and Art (StMWK).

Availability of data and materials

The data sets generated and analyzed during the current study are available from the corresponding author on reasonable request.

Competing interests

The authors declare that they have no competing interests.

Author details

[1] Techincal University Munich, Arcisstr. 21, 80333 Munich, Germany. [2] University of Tubingen, Hölderlinstr. 12, 72072 Tubingen, Germany.

Appendices

Appendix 1

See Table 3.

Table 3 Overview of porosity measurements from different projects for the Malm aquifer in the Bavarian Molasse Basin

Stratigraphy				Outcrop						Outcrop/subsurface				Subsurface													
Epoch	Age	Quenstedt and Richter (1987)	STD (2016)	Hedtmann and Alber (2018)		Mraz et al. (2018)				Homuth (2014)				Dingolfing FB				Limestone[a]	Dolostone[a]	Moosburg SC 4						Pullach (Th 2)[b]	Unterhaching (Gt Uha 1/1a)[c]
														This study[d]						Böhm (2012)		This study[d]					
				Mean	n	Min	Max	Med	n	Min	Max	Med	n	Min	Max	Med ± MAD	n	Min–Max (Med)		Min–Max (Med)	n	Min	Max	Med ± MAD	n	Min–Max (Med)	
Early Cretaceous		Purbeck																				0.5	17.3	4.6 ± 2.5	73	< 3.0 $n=5$	
Late Jurassic	Tithonian	Malm ζ 4–5	Rennertshofen & Usseltal Fm.							< 0.1	17.8	5.1	381	3.3	15.7	10.7 ± 5.1	6	0.7–17.1 (3.8), $n=14$	1.5–6.7 (3.2), $n=9$			3.1	19.2	13.6 ± 4.5	32	5.0–10.0 $n=10$	
		Malm ζ 3	Mörnsheim Fm.			5.6	8.6	7.0	13													2.5	3.9	3.1 ± 0.3	18		9.0 $n=2$
		Malm ζ 2	Altmülthal Fm.			3.7	14.8	7.0	31					1.8	17.7	3.5 ± 1.8	9			0.6–2.1 (0.7)	3	0.3	10.2	5.6 ± 3.4	35		1.0–4.0 (2.5), $n=4$
		Malm ζ 1	Geisental Fm.	5.8	25	4.0	8.5	5.8	21					4.2	12.2	9.2 ± 3.9	5			0.9 – 17.1 (7.3)	5	0.3	18.4	2.1 ± 1.5	32		
	Kimmeridgian	Malm ε	Torleite Fm.			3.6	11.2	6.9	13	0.9	10.4	9.6	81	2.5	12.7	4.6 ± 1.1	19			1.1 – 5.4 (3.3)	2	0.5	5.9	2.9 ± 1.7	19		
		Malm δ	Treuchtlingen Fm.	8.4	28	1.6	6.9	4.6	29	0.4	6.9	2.7	226	2.3	6.3	3.2 ± 0.7	12			2.4 – 7.6 (5.0)	2	0.7	4.7	2.3 ± 1.1	36	< 5.0 $n=3$	6.0–18.0 (14.0), $n=4$
		Malm γ	Arzberg Fm.							< 0.1	7.5	1.8	112							1.4	1	1.1	3.2	2.0 ± 0.3	15		
	Oxfordian	Malm β	Dietfurt Fm.							0.2	10.2	3.3	181									0.4	3.5	2.0 ± 0.3	14		
		Malm α								0.5	9.9	6.2	145									0.3	10.3	1.0 ± 0.5	18		
Middle Jurassic		Dogger ζ																				3.8	15.4	7.9 ± 2.4	20		

[a] Koch et al. (2009), [b]Böhm et al. (2010), [c]Beichel et al. (2014), [d]porosity effective for water ϕ_{eff}^{w}, unit = %, *Min* minimum, *Max* maximum, *Med* median, *MAD* median absolute deviation, *n* count

Appendix 2: Evaluation of WIP and HEP methods

Evaluation of WIP and HEP methods

The porosity data set derived from the investigations on the core samples show a widely scattered distribution in the range between 0.2 and 22.2% with a median of 4.1%. This data set includes data for the effective porosity measured on 363 samples using both the gas expansion method and the water immersion method. The distribution for the $\phi_{\mathrm{eff}}^{\mathrm{He}}$ (HEP method) varies in the same range between 0.2 and 22.2% with a slightly higher median of 4.7%. The $\phi_{\mathrm{eff}}^{\mathrm{w}}$ (WIP method) is distributed between 0.3 and 19.2% with a lower median of 3.4%. Both methods produced a positively skewed distribution and high variance for each lithological group (Fig. 17a). To compare the results of each method and allow prediction of $\phi_{\mathrm{eff}}^{\mathrm{w}}$ measured by the HEP method or vice versa, the deviation of results for each sample has to be evaluated. Figure 17a indicates predominantly higher porosity readings using the HEP method. The deviation of porosity was determined as difference by subtracting HEP results from WIP results, resulting in negative values for higher HEP porosity and positive values for higher WIP porosity. The comparison of porosity deviation shows a rather unimodal distribution with wide range from 6.8% p.u. to 3.1% p.u. and a median of 1.0% p.u. (Fig. 17b). Most of the values (80%) fall within a range of − 2.8 to 0.6% p.u. with 50% of all values between 0.5 and 1.5% p.u. deviation.

Contrary to water, pure helium gas seems to easily penetrate all connected pores including the micropores and thus describing the highest possible value for the effective porosity. Furthermore, saturation by purified water is also limited to the size of pore throats connecting the pores to allow percolation through the rock matrix and can be affected by wettability of the rock matrix. The cohesive and adhesive nature of water impedes flow through narrow pore throats and channels, resulting in lower effective porosity (Stober and Bucher 2013). In addition, the irregular occurrence of vugs and fractures connected to the surface of the plugs produce further negative results by saturation loss when the sample has to be removed from desiccator to determine saturated weight (McPhee et al. 2015).

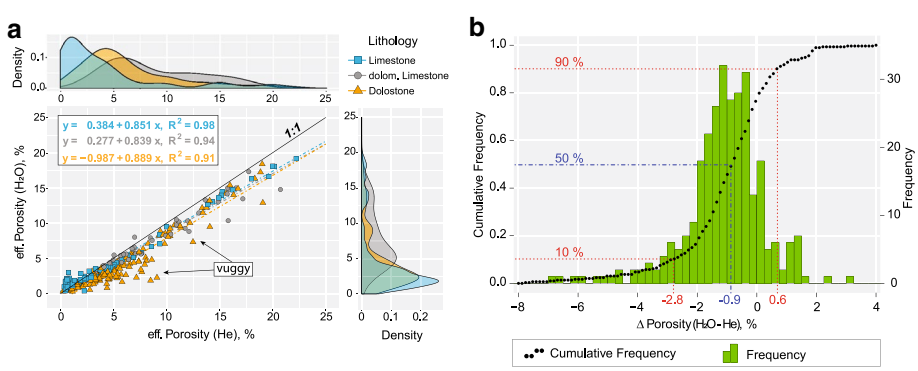

Fig. 17 Comparison of porosity measured by HEP and WIP methods. **a** $\phi_{\mathrm{eff}}^{\mathrm{w}}$ is directly plotted against $\phi_{\mathrm{eff}}^{\mathrm{He}}$. Data were separated to control lithology dependency. Density plots show a positively skewed distribution and a high variance of porosity. B: Histogram and cumulative frequency of porosity deviation between both methods (bin width = 0.25%). Red dotted lines show 10% and 90% percentiles between which most deviation values were found. Blue dashed line indicates that 50% of all samples have a deviation of less than—0.9% p.u. and 50% more than—0.9% p.u

The measurements during this study show the same behavior. Comparing them for each individual sample, the porosity measured by the WIP method is generally lower than that measured by the HEP method (Fig. 17a). The deviation seems to increase with increasing porosity and is mostly negative. However, some samples show a positive deviation, indicating a higher porosity reading by the WIP method. By separating the data set according to lithology of the samples, a positive deviation can be detected almost only for very fine-grained, marly limestone samples with generally low porosity (Fig. 17a). Swelling of clay minerals causing fissures, grain losses during saturation of more friable samples as well as a strong capillarity of the fine-grained material resulting in increased adhesion to liquids on the outside of the sample can be an explanation (McPhee et al. 2015).

Besides relation to lithology, further parameters were controlled on their impact to the porosity deviation between WIP and HEP methods. The results are presented as correlation matrix (Fig. 18) indicating a negative correlation of porosity deviation with porosity itself, lithology, facies, and grain density. Hence, with increasing dolomitization and increasing size of components or crystals, the HEP method should provide higher

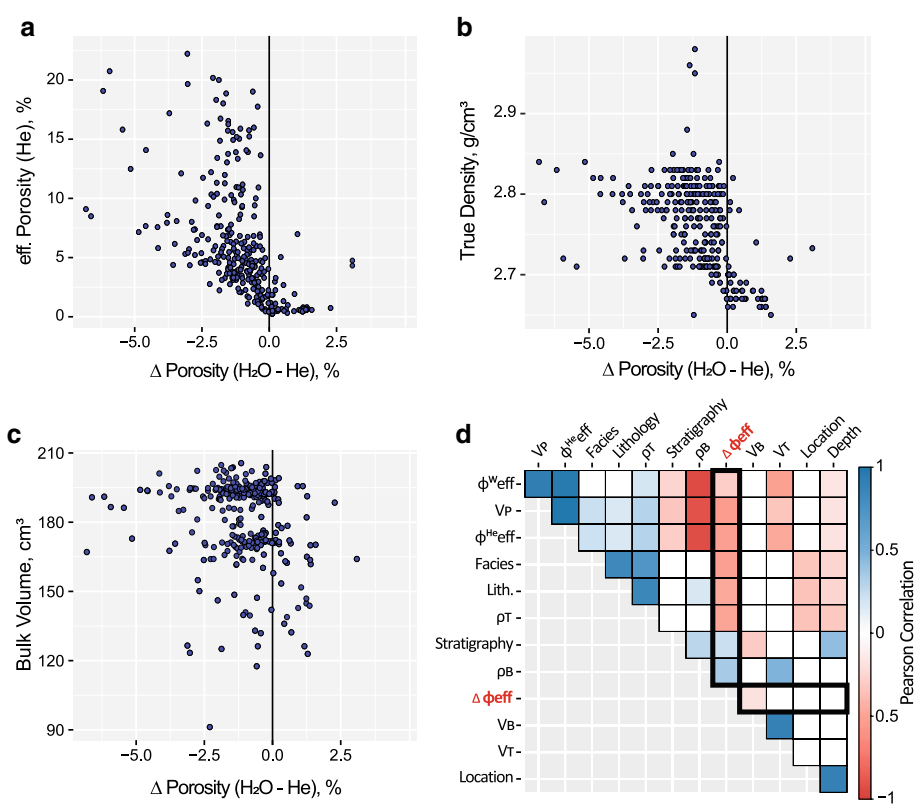

Fig. 18 Dependency of porosity deviation between HEP and WIP methods related to different factors. **a** Porosity deviation becomes increasingly negative with increasing porosity. A positive deviation was mainly found for samples with low porosity. **b** Correlation of the porosity deviation with grain density suggests a dependency on lithology. **c** The porosity deviation seems not to be related to bulk volume (i.e., dimensions) of the sample. **d** The matrix shows the Pearson correlation coefficients of different parameters. Blue color represents a positive correlation, whereas red represents a negative correlation. (ϕ_{eff}^{He} = effective porosity (HEP), ϕ_{eff}^{W} = effective porosity (WIP), ρ_B = bulk density, ρ_T = grain density, V_B = bulk volume, V_T = helium grain volume, V_P = pore volume)

porosity results than the WIP method. Figure 18a, b shows the dependence that with increasing $\phi_{\mathrm{eff}}^{\mathrm{He}}$ as well as increasing ρ_{g} the deviation between the measurements seems to become increasingly negative and vice versa. Other factors like sample volume, sample location, and depth of the rock core do not appear to have a significant impact on the porosity deviation (Fig. 18c, d).

Appendix 3

See Table 4.

Table 4 Distribution of porosity for MSC-4 and DGF-FB grouped by stratigraphic units

Location	Stratigraphy	Rock density, g/cm^3			Grain density, g/cm^3			Porosity (He), %			Porosity (H_2O), %			*n*
		Min	Max	Med ± MAD	Min	Max	Med ± MAD	Min	Max	Med ± MAD	Min	Max	Med ± MAD	
Moosburg SC 4	Purbeck	2.15	2.72	2.59 ± 0.06	2.65	2.85	2.72 ± 0.02	0.3	20.7	5.7 ± 3.2	0.5	17.3	4.6 ± 2.5	73
	Malm ζ 4–5	2.10	2.68	2.52 ± 0.17	2.69	2.85	2.72 ± 0.01	1.2	22.2	7.7 ± 5.2	3.1	19.2	13.6 ± 4.5	32
	Malm ζ 3	2.34	2.64	2.60 ± 0.01	2.71	2.74	2.72 ± 0.01	2.5	14.3	4.4 ± 0.4	2.5	3.9	3.1 ± 0.3	18
	Malm ζ 2	2.43	2.79	2.57 ± 0.08	2.73	2.85	2.80 ± 0.03	0.8	14.0	7.4 ± 3.1	0.3	10.2	5.6 ± 3.4	35
	Malm ζ 1	2.28	2.79	2.71 ± 0.08	2.77	2.83	2.81 ± 0.01	0.2	19.1	3.0 ± 2.5	0.3	18.4	2.1 ± 1.5	32
	Malm ε	2.54	2.75	2.65 ± 0.04	2.77	2.82	2.71 ± 0.01	1.3	8.6	5.7 ± 1.5	0.5	5.9	2.9 ± 1.7	19
	Malm δ	2.55	2.76	2.66 ± 0.01	2.74	2.81	2.79 ± 0.00	1.1	8.5	4.5 ± 0.6	0.7	4.7	2.3 ± 1.1	36
	Malm γ	2.63	2.74	2.65 ± 0.01	2.66	2.82	2.68 ± 0.01	0.5	3.3	1.0 ± 0.4	1.1	3.2	2.0 ± 0.3	15
	Malm β	2.61	2.67	2.63 ± 0.02	2.65	2.70	2.67 ± 0.01	0.3	3.3	1.2 ± 0.7	0.4	3.5	2.0 ± 0.3	14
	Malm α	2.45	2.67	2.66 ± 0.01	2.67	2.79	2.68 ± 0.00	0.3	12.0	0.6 ± 0.1	0.3	10.3	1.0 ± 0.5	18
	Top Dogger	2.32	2.72	2.55 ± 0.10	2.73	2.84	2.77 ± 0.02	4.1	16.3	8.5 ± 2.8	3.8	15.4	7.9 ± 2.4	20
Dingolfing FB	Malm ζ 4–5	2.29	2.64	2.48 ± 0.15	2.71	2.83	2.72 ± 0.01	3.5	15.2	10.3 ± 4.8	3.3	15.7	10.7 ± 5.1	6
	Malm ζ 2	2.22	2.74	2.65 ± 0.05	2.67	2.83	2.80 ± 0.02	2.5	10.4	5.7 ± 1.8	1.8	17.7	3.5 ± 1.8	9
	Malm ζ 1	2.49	2.64	2.54 ± 0.04	2.78	2.98	2.86 ± 0.08	4.9	15.6	12.8 ± 2.8	4.2	12.2	9.2 ± 3.9	5
	Malm ε	2.43	2.79	2.66 ± 0.04	2.73	2.95	2.81 ± 0.02	3.5	13.8	5.5 ± 1.3	2.5	12.7	4.6 ± 1.1	19
	Malm δ	2.57	2.76	2.66 ± 0.02	2.74	2.82	2.80 ± 0.01	1.7	7.8	4.7 ± 1.0	2.3	6.3	3.2 ± 0.7	12

Min minimum, *Max* maximum, *Med* median, *MAD* median absolute deviation, *n* count

Appendix 4

See Table 5.

Table 5 Distribution of measured porosity subject to lithology for MSC-4 and DGF-FB

Location	Lithology	Rock density, g/cm^3			Grain density, g/cm^3			Porosity (He), %			Porosity (H_2O), %			*n*
		Min	Max	Med ± MAD	Min	Max	Med ± MAD	Min	Max	Med ± MAD	Min	Max	Med ± MAD	
Moosburg SC 4	Limestone	2.12	2.70	2.63 ± 0.03	2.65	2.73	2.70 ± 0.02	0.3	22.2	2.3 ± 1.7	0.4	19.2	2.2 ± 1.2	94
	Dolom. limestone	2.15	2.72	2.55 ± 0.09	2.71	2.84	2.75 ± 0.01	2.4	20.7	7.6 ± 3.0	1.8	17.3	6.4 ± 2.3	51
	Dolostone	2.28	2.79	2.65 ± 0.07	2.73	2.85	2.80 ± 0.02	0.2	19.1	4.9 ± 2.5	0.3	18.4	2.6 ± 1.4	100
Dingolfing FB	Limestone	2.29	2.32	2.30 ± 0.01	2.71	2.71	2.71 ± 0.00	14.3	15.2	14.8 ± 0.4	13.0	14.5	13.8 ± 0.7	2
	Dolom. limestone	2.55	2.64	2.61 ± 0.03	2.73	2.73	2.73 ± 0.00	3.4	6.4	4.3 ± 0.8	2.4	5.1	3.1 ± 0.7	3
	Dolostone	2.22	2.79	2.65 ± 0.04	2.67	2.98	2.80 ± 0.01	1.6	15.6	5.5 ± 1.6	1.4	17.0	4.0 ± 1.4	45

Min minimum, *Max* maximum, *Med* median, *MAD* median absolute deviation, *n* count

Appendix 5

See Table 6.

Table 6 Porosity data set for MSC-4 and DGF-FB grouped by facies, crystal size and crystal morphology

Lithology	Facies	Rock density, g/cm^3			Grain density, g/cm^3			Porosity (He), %			Porosity (H_2O), %			*n*
		Min	Max	Med ± MAD	Min	Max	Med ± MAD	Min	Max	Med ± MAD	Min	Max	Med ± MAD	
Limestone	Mudstone	2.52	2.70	2.64 ± 0.03	2.64	2.73	2.69 ± 0.02	0.3	4.6	1.0 ± 1.5	0.4	3.9	1.8 ± 1.0	48
	Wackestone	2.52	2.69	2.64 ± 0.02	2.66	2.73	2.70 ± 0.01	0.3	2.9	1.1 ± 0.8	0.3	2.9	1.9 ± 0.8	15
	Packstone	2.46	2.64	2.57 ± 0.06	2.70	2.71	2.71 ± 0.01	2.5	9.4	5.5 ± 2.1	2.1	7.1	4.6 ± 1.6	8
	Grainstone	2.12	2.65	2.36 ± 0.10	2.58	2.73	2.71 ± 0.02	0.7	22.2	10.0 ± 6.6	1.1	19.2	9.5 ± 6.0	25
Dolom. limestone	Mudstone	2.58	2.69	2.62 ± 0.03	2.72	2.79	2.75 ± 0.01	2.4	4.7	3.3 ± 1.2	1.8	4.4	3.1 ± 1.3	3
	Wackestone	2.32	2.72	2.61 ± 0.02	2.73	2.84	2.76 ± 0.02	4.8	7.6	6.4 ± 1.1	4.1	5.8	4.9 ± 0.7	7
	Packstone	2.36	2.67	2.58 ± 0.06	2.73	2.77	2.76 ± 0.03	3.5	12.0	5.7 ± 1.8	2.4	10.3	5.4 ± 1.7	21
	Grainstone	2.15	2.56	2.36 ± 0.09	2.71	2.80	2.75 ± 0.02	8.5	20.7	13.0 ± 3.2	7.6	17.3	11.7 ± 2.9	21
Dolostone	Fine-X	2.28	2.79	2.67 ± 0.15	2.73	2.88	2.80 ± 0.03	0.2	19.1	3.8 ± 5.2	0.3	18.4	2.6 ± 4.8	67
	Medium-X	2.36	2.79	2.66 ± 0.06	2.67	2.98	2.80 ± 0.03	1.3	15.3	5.2 ± 2.3	0.7	13.8	3.1 ± 2.1	62
	Coarsely X	2.32	2.58	2.52 ± 0.08	2.74	2.97	2.80 ± 0.06	4.5	17.8	10.2 ± 3.3	1.9	16.3	8.2 ± 4.0	20
	Xenomorphic	2.66	2.79	2.74 ± 0.04	2.75	2.82	2.80 ± 0.02	0.2	4.9	1.5 ± 1.3	0.3	4.0	0.7 ± 1.0	12
	Xeno-hypidiomorphic	2.69	2.76	2.72 ± 0.03	2.79	2.81	2.81 ± 0.01	1.6	4.2	3.2 ± 1.0	1.4	2.6	2.0 ± 0.5	12
	Hypidiomorphic	2.49	2.79	2.67 ± 0.05	2.73	2.95	2.80 ± 0.03	0.8	12.5	4.2 ± 2.1	0.5	7.3	2.7 ± 1.6	67
	Hypidio-idiomorphic	2.54	2.71	2.63 ± 0.04	2.76	2.82	2.79 ± 0.01	3.1	9.9	5.6 ± 1.7	1.4	8.6	2.8 ± 1.5	27
	Idiomorphic	2.28	2.67	2.47 ± 0.10	2.67	2.98	2.82 ± 0.06	5.7	19.1	11.8 ± 3.5	4.6	18.4	9.9 ± 3.5	20

Min minimum, *Max* maximum, *Med* median, *MAD* median absolute deviation, *n* count

Appendix 6

See Table 7.

Table 7 Permeability data set for MSC-4 and DGF-FB grouped by stratigraphic units

Location	Stratigraphy	Permeability (core), mD			*n*	Permeability (GPPT model), mD			*n*
		Min	Max	Med ± MAD		Min	Max	Med ± MAD	
Moosburg SC 4	Purbeck	3.0 E−3	1.6 E+0	7.9 E−2 ± 6.1 E−1	6	1.0 E−7	6.2 E+1	4.1 E−3 ± 9.1 E+0	54
	Malm ζ 4–5	1.4 E−1	2.6 E+1	5.9 E+0 ± 1.2 E+1	4	9.6 E−4	1.2 E+2	1.2 E+1 ± 3.7 E+1	23
	Malm ζ 3					4.0 E−4	2.2 E−3	9.5 E−4 ± 5.7 E−4	9
	Malm ζ 2	9.7 E−1	3.5 E+0	2.2 E+0 ± 1.8 E+0	2	1.0 E−7	4.7 E+0	9.2 E−3 ± 1.2 E+0	27
	Malm ζ 1	2.3 E+0	2.1 E+1	3.9 E+0 ± 7.8 E+0	5	1.0 E−7	1.5 E+0	1.6 E−4 ± 3.7 E−1	25
	Malm ε	7.2 E−2	3.3 E+1	1.6 E+1 ± 1.6 E+1	4	6.0 E−7	6.4 E−2	5.8 E−4 ± 1.8 E−2	13
	Malm δ	1.6 E+0	1.7 E+1	2.5 E+0 ± 7.6 E+0	4	1.5 E−6	1.1 E−2	1.5 E−4 ± 2.2 E−3	36
	Malm γ					2.3 E−5	9.9 E−4	1.7 E−4 ± 2.9 E−4	15
	Malm β					4.0 E−7	1.5 E−3	1.8 E−4 ± 4.5 E−4	14
	Malm α					2.0 E−7	7.9 E−2	1.4 E−5 ± 1.9 E−2	18
Dingolfing FB	Malm ζ 4–5	1.3 E−3	2.0 E+1	1.4 E−2 ± 1.1 E+1	3	3.4 E−4	1.9 E+1	2.3 E−1 ± 7.9 E+0	6
	Malm ζ 2	4.0 E−4	7.3 E−1	8.4 E−3 ± 2.7 E−1	7	6.4 E−5	1.6 E+0	6.4 E−3 ± 6.1 E−1	7
	Malm ζ 1	2.2 E+1			1	1.0 E−1	3.7 E+1	1.2 E+1 ± 1.9 E+1	3
	Malm ε	2.0 E−4	2.2 E+1	1.5 E−3 ± 5.8 E+0	15	3.9 E−4	1.2 E+1	3.4 E−3 ± 3.1 E+0	21
	Malm δ	1.0 E−4	1.4 E−2	6.5 E−3 ± 4.6 E−3	6	2.0 E−5	1.8 E−2	9.8 E−4 ± 5.2 E−3	12

Min minimum, *Max* maximum, *Med* median, *MAD* median absolute deviation, *n* count

Appendix 7

See Table 8.

Table 8 Permeability data set subject to lithology for MSC-4 and DGF-FB

Location	Lithology	Permeability (core), mD			*n*	Permeability (GPPT model), mD			*n*
		Min	Max	Med ± MAD		Min	Max	Med ± MAD	
Moosburg SC 4	Limestone	3.0 E−3	2.6 E+1	3.6 E−1 ± 1.1 E+1	5	1.0 E−7	1.2 E+2	2.6 E−4 ± 1.8 E+1	94
	Dolom. limestone	1.0 E−2	5.1 E+0	7.9 E−2 ± 2.5 E+0	4	1.2 E−4	6.2 E+1	7.9 E−2 ± 1.2 E+1	39
	Dolostone	7.2 E−2	3.3 E+1	3.5 E+0 ± 1.0 E+1	16	1.0 E−7	1.0 E+2	2.4 E−4 ± 1.0 E+1	98
Dingolfing FB	Limestone	2.0 E+1			1	9.4 E+0	1.9 E+1	1.4 E+1 ± 6.8 E+0	2
	Dolom. limestone	1.3 E−3			1	3.4 E−4	6.0 E−3	9.4 E−4 ± 3.1 E−3	3
	Dolostone	1.0 E−4	2.2 E+1	6.5 E−3 ± 5.6 E+0	30	2.0 E−5	3.7 E+1	2.5 E−3 ± 6.1 E+0	40

Min minimum, *Max* maximum, *Med* median, *MAD* median absolute deviation, *n* count

Appendix 8

See Table 9.

Table 9 Permeability data set for MSC-4 and DGF-FB grouped by facies, crystal size and crystal morphology

Lithology	Facies	Permeability (core), mD			*n*	Permeability (GPPT model), mD			*n*
		Min	Max	Med ± MAD		Min	Max	Med ± MAD	
Limestone	Mudstone					4.0 E−7	2.2 E−3	1.4 E−4 ± 6.0 E−4	48
	Wackestone					1.0 E−7	7.0 E−4	1.7 E−4 ± 1.9 E−4	15
	Packstone	3.0 E−3			1	9.6 E−5	2.4 E−1	2.7 E−3 ± 7.9 E−2	9
	Grainstone	1.4 E−1	2.6 E+1	6.8 E+0 ± 1.2 E+1	5	8.0 E−7	1.2 E+2	8.2 E−1 ± 3.3 E+1	24
Dolom. limestone	Mudstone	1.0 E−2			1	1.2 E−4	3.5 E−3	9.5 E−4 ± 1.8 E−3	3
	Wackestone	1.3 E−3	8.9 E−2	4.5 E−2 ± 6.2 E−2	2	3.4 E−7	7.9 E−2	4.8 E−3 ± 2.1 E−2	13
	Packstone					276 E−3	9.6 E−3	5.0 E−3 ± 2.8 E−3	7
	Grainstone	7.0 E−2	5.1 E+0	2.6 E+0 ± 3.5 E+0	2	4.4 E−1	6.2 E+1	4.7 E+0 ± 1.5 E+1	19
Dolostone	FinE-X	2.0 E−4	2.1 E+1	3.4 E−3 ± 4.4 E+0	20	1.0 E−7	1.5 E+0	9.8 E−4 ± 2.5 E−1	65
	Medium-X	1.0 E−4	2.2 E+1	9.7 E−1 ± 6.0 E+0	12	1.1 E−5	8.4 E−2	3.9 E−4 ± 1.8 E−2	49
	Coarsely X	4.9 E−2	3.3 E+1	5.6 E+0 ± 1.3 E+1	10	5.5 E−6	1.0 E+2	3.3 E−3 ± 2.1 E+1	28
	Xenomorphic					1.0 E−7	1.6 E−4	1.9 E−6 ± 4.6 E−5	12
	Xenohypidiomorphic	8.4 E−3	7.2 E−2	4.0 E−2 ± 4.5 E−2	2	6.0 E−7	3.9 E−4	4.1 E−5 ± 1.4 E−4	12
	Hypidiomorphic	1.0 E−4	3.3 E+1	4.5 E−3 ± 7.7 E+0	22	1.5 E−6	4.9 E−2	4.4 E−4 ± 6.5 E−3	67
	Hypidioidiomorphic	2.0 E−4	2.7 E+1	1.7 E+0 ± 9.8 E+0	9	1.7 E−4	2.4 E−1	3.5 E−3 ± 4.6 E−2	27
	Idiomorphic	1.4 E−2	2.2 E+1	3.7 E+0 ± 7.4 E+0	9	4.8 E−2	1.0 E+2	7.1 E−1 ± 2.3 E+1	20

Min minimum, *Max* maximum, *Med* median, *MAD* median absolute deviation, *n* count)

Received: 2 November 2019 Accepted: 26 March 2020
Published online: 07 April 2020

References

American Petroleum Institute. Recommended practice for core analysis: recommended practice 40. 2nd ed. Washington, D.C.: American Petroleum Institute (API); 1998.

Anovitz LM, Cole DR. Characterization and analysis of porosity and pore structures. Rev Mineral Geochem. 2015;80(1):61–164. https://doi.org/10.2138/rmg.2015.80.04.

Archie GE. The electrical resistivity log as an aid in determining some reservoir characteristics. Trans Am Inst Mech Eng. 1942;146(01):54–67. https://doi.org/10.2118/942054-g.

Arif M, Abu-Khamsin SA, Zhang Y, Iglauer S. Experimental investigation of carbonate wettability as a function of mineralogical and thermo-physical conditions. Fuel. 2020;264:116846. https://doi.org/10.1016/j.fuel.2019.116846.

ASTM Standard D4543. Standard practices for preparing rock core as cylindrical test specimens and verifying conformance to dimensional and shape tolerances (Withdrawn 2017) 2008. West Conshohocken: ASTM International: ASTM International. https://doi.org/10.1520/d4543-08e01.

Bachmann GH, Müller M, Weggen K. Evolution of the Molasse Basin (Germany, Switzerland). Tectonophysics. 1987;137(1–4):77–92. https://doi.org/10.1016/0040-1951(87)90315-5.

BayGLA, editor. Erläuterungen zur Geologischen Karte von Bayern 1:500.000. 4th ed. München: Bayerisches Geologisches Landesamt; 1996.
BayStMivt. Bayerischer Geothermieatlas: Hydrothermale Energiegewinnung. München: Bayerisches Staatsministerium für Wirtschaft, Infrastruktur, Verkehr und Technologie; 2012.
Bear J. Dynamics of Fluids in Porous Media. Reprint. Originally published: New York: American Elsevier. Pub. Co., 1972. Originally published in series: Environmental science series (New York, 1972). With corrections. New York: Dover Publ; 2013.
Beichel K, Koch R, Wolfgramm M. Die Analyse von Spülproben zur Lokalisierung von Zuflusszonen in Geothermiebohrungen. Beispiel der Bohrungen Gt Unterhaching 1/1a und 2 (Süddeutschland, Molassebecken, Malm). Geologische Blätter für Nordost-Bayern. 2014;64(1–4):43–65.
Berg RR. Method for determining permeability from reservoir rock properties. Trans Gulf Coast Assoc Geol Soc. 1970;20:303–17.
Berg RR. Capillary pressures in stratigraphic traps. AAPG Bull. 1975;59(6):939–56. https://doi.org/10.1306/83d91ef7-16c7-11d7-8645000102c1865d.
Birner J, Mayer C, Thomas L, Schneider M, Baumann T, Winkler A. Hydrochemie und Genese der tiefen Grundwässer des Malmaquifers im bayerischenTeil des süddeutschen Molassebeckens. Z Geol Wiss. 2011;39(3/4).
Böhm F. Die Lithofazies des Oberjura (Malm) im Großraum München und deren Einfluss auf die tiefengeothermische Nutzung [Dissertation]. FU Berlin: Freie Universität Berlin; 2012.
Böhm F, Koch R, Höferle R, Baasch R. Der Malm Geothermiebohrung Pullach Th2-Faziesanalyse aus Spülproben (München, S-Deutschland). Geologische Blätter für Nordost-Bayern. 2010;60:79–112.
Böhm F, Birner J, Steiner U, Koch R, Sobott R, Schneider M, Wang A. Tafelbankiger Dolomit in der Kernbohrung Moosburg SC4: Ein Schlüssel zum Verständnis der Zuflussraten in Geothermiebohrungen (Östliches Molassebecken, Malm Delta-Zeta Süddeutschland). Z Geol Wiss. 2011;39:117–57.
Böhm F, Savvatis A, Steiner U, Schneider M, Koch R. Lithofazielle Reservoircharakterisierung zur geothermischen Nutzung des Malm im Großraum München. Grundwasser. 2013;18(1):3–13. https://doi.org/10.1007/s00767-012-0202-4.
Borai AM. A new correlation for the cementation factor in low-porosity carbonates. SPE Form Eval. 1987;2(04):495–9. https://doi.org/10.2118/14401-pa.
Brehme M, Blöcher G, Cacace M, Kamah Y, Sauter M, Zimmermann G. Permeability distribution in the Lahendong geothermal field: a blind fault captured by thermal–hydraulic simulation. Environ Earth Sci. 2016;75(14):577. https://doi.org/10.1007/s12665-016-5878-9.
Büchi UP, Lemcke K, Wiener G, Zimdars J. Geologische Ergebnisse der Erdölexploration auf das Mesozoikum im Untergrund des schweizerischen Molassebeckens. Bull Ver Schweiz Petroleum-Geol U Ing. 1965;32(82):7–38.
Cacace M, Jacquey AB. Flexible parallel implicit modelling of coupled thermal–hydraulic–mechanical processes in fractured rocks. Solid Earth. 2017;8(5):921–41. https://doi.org/10.5194/se-8-921-2017.
Carman PC. Fluid flow through granular beds. Trans Inst Chem Eng. 1937;15:155–66.
Cherubini Y, Cacace M, Blöcher G, Scheck-Wenderoth M. Impact of single inclined faults on the fluid flow and heat transport: results from 3-D finite element simulations. Environ Earth Sci. 2013;70(8):3603–18. https://doi.org/10.1007/s12665-012-2212-z.
Darcy H. Les fontaines publiques de la ville de Dijon. Paris: Victor Dalmont; 1856.
Dufter C, Reinhold N, Kleinertz B, von Roon S. Wärmewende München 2040–Handlungsempfehlungen: Endbericht. München: Forschungsgesellschaft für Energiewirtschaft mbH (FfE); 2018.
Dunham RJ. Classification of carbonate rocks according to depositional texture. In: Ham WE, editor. Classification of carbonate rocks: a symposium. 6th ed. Tulsa: American Association of Petroleum Geologists; 1978. p. 108–21.
Eaton TT. On the importance of geological heterogeneity for flow simulation. Sediment Geol. 2006;184(3–4):187–201. https://doi.org/10.1016/j.sedgeo.2005.11.002.
Ehrlich R, Kennedy SK, Crabtree SJ, Cannon RL. Petrographic image analysis, I. Analysis of reservoir pore complexes. SEPM JSR. 1984. https://doi.org/10.1306/212f85df-2b24-11d7-8648000102c1865d.
Essley PL. What is reservoir engineering? J Petrol Technol. 2013;17(01):19–25. https://doi.org/10.2118/920-PA.
Filomena CM, Hornung J, Stollhofen H. Assessing accuracy of gas-driven permeability measurements: a comparative study of diverse Hassler-cell and probe permeameter devices. Solid Earth. 2014;5(1):1–11. https://doi.org/10.5194/se-5-1-2014.
Flügel E, Munnecke A. Microfacies of carbonate rocks: analysis, interpretation and application. 2nd ed. Berlin: Springer; 2010.
Focke JW, Munn D. Cementation exponents in middle eastern carbonate reservoirs. SPE Form Eval. 1987;2(02):155–67. https://doi.org/10.2118/13735-PA.
Folk RL. Petrology of sedimentary rocks. Austin: Hemphill Pub. Co; 1974.
Fritzer T. Bayerischer Geothermieatlas—Hydrothermale Energiegewinnung: Technik, wirtschaftliche Aspekte, Risiken; hydrothermale Grundwasserleiter in Bayern; Untergrundtemperaturen in Bayern. München: StMWIVT; 2012.
Glover PW, Zadjali II, Frew KA. Permeability prediction from MICP and NMR data using an electrokinetic approach. Geophysics. 2006;71(4):F49–60. https://doi.org/10.1190/1.2216930.
Goldbrunner JE, Vasvári V. Hydrogeology and geothermic simulation of the geothermal doublet at Waldkraiburg (Bavaria). AJES. 2016. https://doi.org/10.17738/ajes.2016.0007.
Hedtmann N, Alber M. Investigation of water-permeability and ultrasonic wave velocities of german malm aquifer rocks for hydro-geothermal energy. Procedia Eng. 2017;191:127–33. https://doi.org/10.1016/j.proeng.2017.05.163.
Hedtmann N, Alber M. Variation of laboratory test results with specimen size in carbonates of Bavarian Malm. Conference Paper, Eurock 2018, St. Petersburg. 2018.
Hommel J, Coltman E, Class H. Porosity–permeability relations for evolving pore space: a review with a focus on (bio-)geochemically altered porous media. Transp Porous Media. 2018;124(2):589–629. https://doi.org/10.1007/s11242-018-1086-2homuth.
Homuth S. Aufschlussanalogstudie zur Charakterisierung oberjurassischer Geothermischer Karbonatreservoire im Molassebecken [Dissertation]. Darmstadt: Technische Universität Darmstadt; 2014.

Homuth S, Götz AE, Sass I. Lithofacies and depth dependency of thermo- and petrophysical rock parameters of the Upper Jurassic geothermal carbonate reservoirs of the Molasse Basin. Zeitschrift der Deutschen Gesellschaft für Geowissenschaften. 2014;165(3):469–86. https://doi.org/10.1127/1860-1804/2014/0074.
Homuth S, Götz AE, Sass I. Physical properties of the geothermal carbonate reservoirs of the Molasse Basin, Germany—outcrop analogue vs. reservoir data. In: Proceedings world geothermal congress, Melbourne, Australia, 19–25 April 2015. 2015.
Jacquey AB, Urpi L, Cacace M, Blöcher G, Zimmermann G, Scheck-Wenderoth M. Far field poroelastic response of geothermal reservoirs to hydraulic stimulation treatment: theory and application at the Groß Schönebeck geothermal research facility. Int J Rock Mech Min Sci. 2018;110:316–27. https://doi.org/10.1016/j.ijrmms.2018.08.012.
Jennings JW, Lucia FJ. Predicting permeability from well logs in carbonates with a link to geology for interwell permeability mapping. SPE Reserv Eval Eng. 2003;6(04):215–25. https://doi.org/10.2118/84942-PA.
Klinkenberg LJ. The permeability of porous media to liquids and gases. Drilling and Production Practice. Washington, DC: American Petroleum Institute; 1941. p. 200–13.
Koch R. Daten zur Fazies und Diagenese von Massenkalken und ihre Extrapolation nach Süden bis unter die Nördlichen Kalkalpen. Geologische Blätter für Nordost-Bayern. 1997;47(1–4):117–50.
Koch R. Die neue Interpretation der Massenkalke des Süddeutschen Malm und ihr Einfluß auf die Qualität von Kalksteinen für technische Anwendungen. Archaeopterix. 2000;18:43–65.
Koch R, Munnecke A. Fazielle Entwicklung und Korrelation des Oberjura in den Bohrungen Bad Waldsee GB2 und Altensteig 1 (Süddeutschland; Molasse-Becken; Impressamergel- bis hangende Bankkalk-Formation). Geologische Blätter für Nordost-Bayern. 2016;66:165–203.
Koch R, Senowbari-Daryan B, Strauss H. The late jurassic 'Massenkalk fazies' of Southern Germany: calcareous sand piles rather than organic reefs. Facies. 1994;31(1):179–208. https://doi.org/10.1007/BF02536939.
Koch R, Bachmann GH, Müller M. Fazies des Oberen Jura (Malm) der Bohrungen Scherstetten 1 und 2 (Molasse-Becken, Süddeutschland) und ihre Bedeutung für die geothermische Exploration. Z Geol Wiss. 2010;38:327–51.
Koltermann CE, Gorelick SM. Heterogeneity in sedimentary deposits: a review of structure-imitating, process-imitating, and descriptive approaches. Water Resour Res. 1996;32(9):2617–58. https://doi.org/10.1029/96WR00025.
Konrad F, Savvatis A, Wellmann F, Zosseder K. Hydraulic behavior of fault zones in pump tests of geothermal wells: a parametric analysis using numerical simulations for the Upper Jurassic aquifer of the North Alpine Foreland Basin. Geotherm Energy. 2019;7(1):129. https://doi.org/10.1186/s40517-019-0137-4.
Koponen A, Kataja M, Timonen J. Permeability and effective porosity of porous media. Phys Rev E. 1997;56(3):3319–25. https://doi.org/10.1103/PhysRevE.56.3319.
Koschel G. Geologischer Überblick-Hydrogeologische Rahmenbedingungen. In: Bayr. LFW & LGRB München, ed. Hydrogeothermische Energiebilanz und Grundwasserhaushalt des Malmkarstes im süddeutschen Molassebecken. Schlussbericht zum Forschungsvorhaben 03E – 6240 A/B (im Auftrag des Bundesministeriums für Forschung und Technologie). Freiburg; 1991. p. 12.
Kozeny J. Über kapillare Leitung des Wassers im Boden: (Aufstieg, Versickerung und Anwendung auf die Bewässerung). Sitzungsber Akad Wiss Wien. 1927;136(2a):271–306.
Kumari W, Ranjith PG. Sustainable development of enhanced geothermal systems based on geotechnical research—a review. Earth Sci Rev. 2019. https://doi.org/10.1016/j.earscirev.2019.102955.
Lemcke K. Das bayerische Alpenvorland vor der Eiszeit: Erdgeschichte-Bau-Bodenschätze. Stuttgart: Schweizerbart; 1988.
Lucia FJ. Petrophysical parameters estimated from visual descriptions of carbonate rocks: a field classification of carbonate pore space. J Petrol Technol. 1983;35(03):629–37. https://doi.org/10.2118/10073-PA.
Lucia FJ. Rock-fabric/petrophysical classification of carbonate pore space for reservoir characterization. Bulletin. 1995. https://doi.org/10.1306/7834d4a4-1721-11d7-8645000102c1865d.
Lucia FJ. Origin and petrophysics of dolostone pore space. Geol Soc Lond Spec Publ. 2004;235(1):141–55. https://doi.org/10.1144/GSL.SP.2004.235.01.06.
Lucia FJ. Carbonate reservoir characterization: an integrated approach. Berlin: Springer; 2007.
Lucia FJ, Conti RD. Rock fabric, permeability, and log relationships in an upward-shoaling, vuggy carbonate sequence: University of Texas at Austin, Bureau of Economic Geology. Geological Circular 87-5; 1987.
Lucia FJ, Kerans C, Senger RK. Defining flow units in dolomitized carbonate-ramp reservoirs: SPE annual technical conference and exhibition, 4–7 October, Washington, D.C.: Society of Petroleum Engineers; 1992. https://doi.org/10.2118/24702-ms.
Lucia FJ, Jennings J, Rahnis M, Meyer FO. Permeability and rock fabric from wireline logs, Arab-D reservoir, Ghawar field, Saudi Arabia. GeoArabia. 2001;6:619–46.
Mahjour SK, Al-Askari MKG, Masihi M. Identification of flow units using methods of Testerman statistical zonation, flow zone index, and cluster analysis in Tabnaak gas field. J Petrol Explor Prod Technol. 2016;6(4):577–92. https://doi.org/10.1007/s13202-015-0224-4.
McPhee C, Reed J, Zubizarreta I. Core analysis: a best practice guide. Amsterdam: Elsevier; 2015.
Menning M, Hendrich A. STD 2016: Stratigraphische Tabelle von Deutschland. 2nd ed. Potsdam: Deutsches GeoForschungsZentrum; 2016.
Meyer RKF, Schmidt-Kaler H. Paläogeographie und Schwammriffentwicklung des süddeutschen Malm—ein Überblick. Facies. 1990a;23(1):175–84.
Meyer RKF, Schmidt-Kaler H. Paläogeographischer Atlas des süddeutschen Oberjura (Malm). Stuttgart: Schweizerbart Science Publishers; 1990b.
Meyer RKF. "Moosburg 4", die erste Kernbohrung durch den Malm unter der bayerischen Molasse. Erlanger Geol Abh. 1994;123:51–81.
Meyer RKF, Schmidt-Kaler H. Jura. In: BayGLA, editors. Erläuterungen zur Geologischen Karte von Bayern 1:500.000. 4th ed. München: Bayerisches Geologisches Landesamt; 1996.
Mraz E. Reservoir characterization to improve exploration concepts of the Upper Jurassic in the Southern Bavarian Molasse Basin [Dissertation]. München: Technische Universität München; 2019. http://nbn-resolving.de/urn/resolver.pl?urn:nbn:de:bvb:91-diss-20190430-1464081-1-6.

Mraz E, Bohnsack D, Stockinger G, Käsling H, Zosseder K, Thuro K. Die Bedeutung von Analogaufschlüssen des Oberjura für die Interpretation der Lithologie der geothermalen Tiefbohrung Geretsried. Jber Mitt oberrhein geol Ver. 2018;2018(100):517–48. https://doi.org/10.1127/jmogv/100/0016.
Nelson PH. Permeability-porosity relationships in sedimentary rocks. Log Anal. 1994;3:38–62.
Niebuhr B. Lithostratigraphie der Weißjura-Gruppe der Frankenalb (außeralpiner Oberjura) und der mittel- bis oberjurassischen Reliktvorkommen zwischen Straubing und Passau (Bayern): Beitrag zur Stratigraphie von Deutschland. Hannover: Dt. Ges. für Geowiss; 2014.
Okotie S, Ikporo B. Reservoir engineering: fundamentals and applications. Cham: Springer International Publishing; 2019.
Quenstedt FA, Richter AE. Der Jura. Korb: Goldschneck-Verl. Weidert; 1987.
Rashid F, Glover P, Lorinczi P, Collier R, Lawrence J. Porosity and permeability of tight carbonate reservoir rocks in the north of Iraq. J Petrol Sci Eng. 2015;133:147–61. https://doi.org/10.1016/j.petrol.2015.05.009.
Scheck-Wenderoth M, Cacace M, Maystrenko YP, Cherubini Y, Noack V, Kaiser BO, et al. Models of heat transport in the Central European Basin System: effective mechanisms at different scales. Mar Petrol Geol. 2014;55:315–31. https://doi.org/10.1016/j.marpetgeo.2014.03.009.
Schlumberger Oilfield Glossary. Porosity unit - Schlumberger Oilfield Glossary. 2018. https://www.glossary.oilfield.slb.com/Terms/p/porosity_unit.aspx. Accessed 16 Aug 2018.
Sibley DF. The origin of common dolomite fabrics: clues from the pliocene. J Sediment Petrol. 1982;52(4):1087–100.
Sibley DF, Gregg J. Classification of dolomite rock textures. J Sediment Petrol. 1987;57:967–75.
Steiner U, Savvatis A, Böhm F, Schubert A. Explorationsstrategie tiefer geothermischer Ressourcen am Beispiel des süddeutschen Oberjuras (Malm). 2014:429–61. https://doi.org/10.1007/978-3-642-54511-5_13.
Stier P, Prestel R. Der Malmkarst im süddeutschen Molassebecken - Ein hydrogeologischer Überblick. In: Bayr. LFW & LGRB München, ed. Hydrogeothermische Energiebilanz und Grundwasserhaushalt des Malmkarstes im süddeutschen Molassebecken. Schlussbericht zum Forschungsvorhaben 03E — 6240 A/B (im Auftrag des Bundesministeriums für Forschung und Technologie). Freiburg; 1991.
Stober I, Bucher K. Geothermal energy: from theoretical models to exploration and development. Berlin: Springer; 2013.
Stober I, Wolfgramm M, Birner J. Hydrochemie der Tiefenwässer in Deutschland—hydrochemistry of deep waters in Germany. Z Geol Wiss. 2014;41/42(5-6) 2013/2014.
Tanikawa W, Shimamoto T. Klinkenberg effect for gas permeability and its comparison to water permeability for porous sedimentary rocks. Hydrol Earth Syst Sci Discuss. 2006;3(4):1315–38. https://doi.org/10.5194/hessd-3-1315-2006.
Tucker ME, Wright VP. Carbonate sedimentology. Oxford: Blackwell Publishing Ltd; 1990.
Ueckert M, Baumann T. Hydrochemical aspects of high-temperature aquifer storage in carbonaceous aquifers: evaluation of a field study. Geotherm Energy. 2019;7(1):50. https://doi.org/10.1186/s40517-019-0120-0.
Wagner W, Pruß A. The IAPWS formulation 1995 for the thermodynamic properties of ordinary water substance for general and scientific use. J Phys Chem Ref Data. 2002;31(2):387–535. https://doi.org/10.1063/1.1461829.
Waxman MH, Smits L. Electrical conductivities in oil-bearing shaly sands. Soc Petrol Eng J. 1968;8(02):107–22. https://doi.org/10.2118/1863-A.

Publisher's Note

Springer Nature remains neutral with regard to jurisdictional claims in published maps and institutional affiliations.

Submit your manuscript to a SpringerOpen journal and benefit from:

- ► Convenient online submission
- ► Rigorous peer review
- ► Open access: articles freely available online
- ► High visibility within the field
- ► Retaining the copyright to your article

Submit your next manuscript at ► springeropen.com